Supplemental Material (SM):
Microscopic Mechanisms and Dual Pathways of 5f Electron Itinerancy Tuned by Ligand Chemistry and Pressure in Paramagnetic Uranium Dipnictides

Reyhaneh Ebrahimi-Jaberi[1] and S. Jalali-Asadabadi[1,*]

[1]Department of Physics, Faculty of Physics, University of Isfahan (UI), Hezar Jerib Avenue, Isfahan 8174673441, Iran

This Supplemental Material (SM) accompanies the main article, *"Microscopic Mechanisms and Dual Pathways of $5f$ Electron Itinerancy Tuned by Ligand Chemistry and Pressure in Paramagnetic Uranium Dipnictides"*, and provides additional methodological details and extended analyses that support the results presented in the main manuscript. Because the main article necessarily presents many aspects of the study in a compact and integrated form through representative figures and concise discussions, the SM expands on selected topics by examining specific results in greater detail and by providing supporting data that could not be included in the primary text due to space limitations. In particular, the SM extends the discussion of numerical convergence presented in Appendix A AIV of the main paper by providing additional diagnostics for the charge–self–consistent DFT+DMFT calculations. Furthermore, it presents a comprehensive analysis of the uranium $5f$ electronic structure of UP_2 in its experimentally determined $I4/mmm$ crystal structure, corresponding to the full content of Appendix B of the main manuscript. This includes detailed spectral functions, densities of states, valence-state histograms, and thermodynamic observables under both ambient and compressed conditions. In addition, the SM provides a self-contained clarification of the uranium atomic-term hierarchy, explicitly distinguishing the many-electron $^5L_6$ atomic ground multiplet from the one-electron relativistic $5f$ basis used in the DFT+DMFT implementation. In this computational basis, the 14-dimensional $5f$ shell is organized into $j = 5/2$ and $j = 7/2$ sectors and, in the strong-SOC tetragonal limit, into seven Kramers doublets. The SM also documents the symmetry reduction and solver-input construction of the hybridization function, tracing the workflow from `case.dlt1` through `sjoin.py` and `Delta.imp` to `Delta.inp`, and further presents the operator-based procedure used to extract paramagnetic local moments from CT-QMC probability distributions. By expanding these specific components and presenting more detailed analyses, the SM provides a deeper technical and physical foundation for the hybridization-controlled picture of $5f$ itinerancy developed in the main article.

CONTENTS

* Corresponding author: sjalali@sci.ui.ac.ir

SMI. INTRODUCTION

This document constitutes the Supplemental Material (SM) for the main article entitled *"Microscopic Mechanisms and Dual Pathways of* $5f$ *Electron Itinerancy Tuned by Ligand Chemistry and Pressure in Paramagnetic Uranium Dipnictides"*. The main manuscript presents a unified investigation of the electronic structure of UX_2 (X = P, As, Sb), demonstrating how uranium–ligand hybridization governs the degree of itinerancy of the U $5f$ electrons and how this behavior can be tuned through two complementary mechanisms: ligand substitution and hydrostatic pressure. To emphasize the central physical picture, the main article presents many aspects of the results in a compact and integrated form using representative figures and concise discussions.

Because of the limited space available in the main manuscript, several technical details and extended analyses are necessarily summarized there. The purpose of this Supplemental Material (SM) is therefore to provide a more detailed presentation of selected aspects of the study and to supply additional supporting results that reinforce the conclusions of the main work.

First, the SM expands upon part of the convergence analysis introduced in Appendix A AIV of the main paper. In particular, we provide a more detailed examination of the numerical stability of the charge–self–consistent DFT+DMFT calculations by presenting diagnostics of both the outer charge–self–consistent cycle and the inner DMFT impurity loop. These results demonstrate the robustness of the computational procedure and confirm that the electronic structures reported in the main manuscript are obtained from fully converged paramagnetic solutions at $T = 300$ K.

Second, the SM contains a comprehensive presentation of the results associated with Appendix B in the main paper, including Apendices B BI and B BII of the main paper, which concerns the electronic structure of UP_2 in its experimentally determined $I4/mmm$ crystal structure. While the main manuscript primarily employs the unified $P4/nmm$ reference structure to facilitate systematic comparisons across the UX_2 series, the analysis presented here examines the $I4/mmm$ phase in detail. We present extended momentum-resolved spectral functions, spin–orbit–resolved densities of states, valence-state histograms, and thermodynamic diagnostics including the average $5f$ occupancy $\langle n_{5f} \rangle$, the local magnetic susceptibility χ_{loc}, and the dynamical local moment μ_{U}, both at ambient pressure and under hydrostatic compression.

Third, the SM clarifies the hierarchy of descriptions relevant to the uranium $5f$ shell. At the many-electron atomic level, the free-ion ground term is $^5L_6$, whereas in the relativistic one-electron basis used in DFT+DMFT the 14-dimensional $5f$ shell separates into $j = 5/2$ and $j = 7/2$ sectors with dimensions six and eight, respectively. Under tetragonal symmetry in the strong-SOC limit, these relativistic sectors further split into seven Kramers doublets. This distinction is important for connecting the atomic discussion to the correlated basis actually used in the calculations.

Fourth, the SM documents the construction and use of the hybridization function in explicit workflow form. Section SMV shows how the matrix-valued hybridization output of the DFT+DMFT cycle is reduced into symmetry-resolved channels through `sjoin.py`, stored in `Delta.imp`, reformatted by `ctqmc.py` into `Delta.inp`, and then reconstructed internally within the CT-QMC solver. This makes precise the provenance of the hybridization quantities analyzed in the main text and clarifies that they represent symmetry-reduced channels rather than the unreduced full hybridization matrix.

Finally, the SM provides an explicit operator-based workflow for evaluating the paramagnetic local moment from the CT-QMC impurity solution. This includes the activation of the corresponding sampling mode, the accumulation of impurity-state probabilities, and the post-processing procedure used to obtain the reported root-mean-square longitudinal moment from the impurity density matrix, as documented in Sec. SMVI.

By providing a more comprehensive analysis of the $I4/mmm$ phase of UP_2 and additional convergence diagnostics for the DFT+DMFT calculations, the SM complements the compact presentation of the main manuscript. These methodological additions also strengthen the transparency and reproducibility of the computational workflow and make more explicit the connection between the atomic, hybridization-resolved, and impurity-solver levels of description. These extended results further substantiate the central conclusion of the study: that uranium–ligand hybridization plays the dominant role in controlling the degree of $5f$ itinerancy in UX_2, while external pressure provides an additional pathway for tuning the hybridization strength and the resulting electronic correlations.

SMII. NUMERICAL CONVERGENCE AND STABILITY OF THE OUTER CHARGE–SELF–CONSISTENT DFT+DMFT CYCLE

The charge–self–consistent DFT+DMFT calculations are performed through a hierarchical iterative procedure consisting of two nested self-consistent loops. The first level is the outer DFT+DMFT cycle, which updates the lattice charge density and the Kohn–Sham electronic structure. Embedded

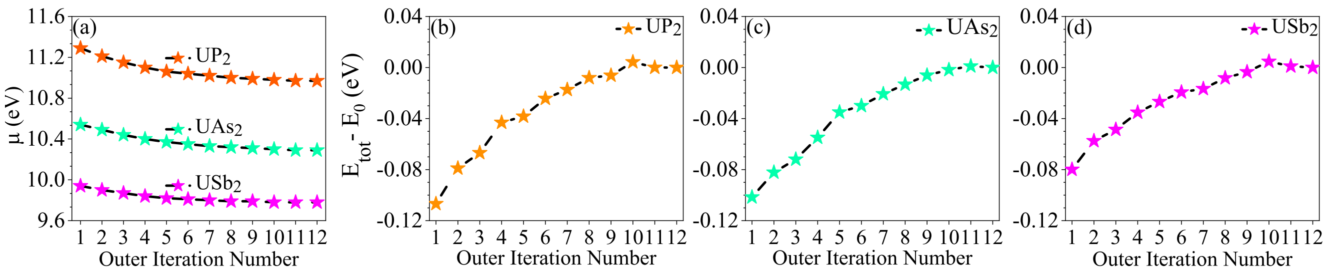

FIG. SM1. Convergence of the outer (global) charge–self–consistent DFT+DMFT loop including SOC at zero pressure for UP_2, UAs_2, and USb_2. The evolution of the chemical potential μ and the total energy relative to the final converged value, $E_{tot} - E_0$, is shown as a function of the *outer* DFT+DMFT iteration number, where E_0 denotes the total energy at the final outer iteration. Panel (a) displays the behavior of μ during the full charge–self–consistent cycle, while panels (b–d) present the corresponding relative total energies $E_{tot} - E_0$ for the three compounds. In all materials, μ and $E_{tot} - E_0$ exhibit an initial transient regime and subsequently approach a well-defined plateau by iterations ∼8–10, indicating convergence of the full charge–self–consistent DFT+DMFT cycle, with the remaining energy variations lying within the adopted total-energy convergence threshold of 10^{-5} Ry (see Sec. SMIV).

within this cycle is a second, faster inner DMFT loop that determines the correlated impurity self-energy for the current electronic environment. The two loops operate on different levels of the calculation and therefore exhibit distinct convergence behavior.

Figure SM1 characterizes the convergence of the outer charge–self–consistent DFT+DMFT loop. In this global cycle the DFT electronic structure (through the LAPW steps) and the DMFT impurity solution are repeatedly coupled until a stable electronic charge density and interacting Fermi level are obtained. The chemical potential μ and the total energy relative to the final converged value, $E_{tot} - E_0$, provide sensitive indicators of this global convergence because they reflect the combined effect of the Kohn–Sham potential, the correlated DMFT self-energy, and the charge redistribution between successive iterations.

Figure SM1(a) shows the evolution of the chemical potential as a function of the outer iteration number for UP_2, UAs_2, and USb_2. In all three systems μ evolves smoothly during the first few iterations and subsequently approaches a stationary value. After approximately 8–10 iterations the changes in μ become negligible, indicating that the interacting Fermi level and the charge density have reached a stable self-consistent solution.

A similar behavior is observed for the relative total energy $E_{tot} - E_0$ shown in Figs. SM1(b)–SM1(d). The initial iterations correspond to a transient regime in which the electronic charge density and the correlated self-energy adjust to one another. As the calculation proceeds, the total energy gradually stabilizes and forms a clear plateau. The simultaneous saturation of μ and $E_{tot} - E_0$ demonstrates that the full DFT+DMFT charge–self–consistent cycle has converged.

The converged chemical potential extracted from this plateau defines the Fermi level used to set the zero of energy when constructing the momentum-resolved spectral functions of the UX_2 compounds in the $P4/nmm$ phase at zero pressure, shown in Figs. 3(a)–(c) of the main paper. The same procedure, not shown here, was also applied for the spectra in the $P4/nmm$ phase under pressure [Figs. 3(d)–(f) of the main paper], as well as for the UP_2 compound in the $I4/mmm$ phase at zero pressure [Fig. B2(a)] and at $P = 4.427$ GPa [Fig. B2(b) of the main paper]. Consequently, the Fermi-level alignment in all spectra follows directly from the fully self-consistent DFT+DMFT solution.

All calculations were performed in the PM regime at $T = 300$ K, well above the Néel temperatures of UP_2, UAs_2, and USb_2 [1–3]. The plateau behavior observed in Fig. SM1 therefore confirms that the spectral features discussed in this work originate from a numerically stable DFT+DMFT solution.

SMIII. NUMERICAL CONVERGENCE AND STABILITY OF THE INNER DMFT IMPURITY LOOP

While Fig. SM1 monitors the convergence of the global DFT+DMFT cycle, Fig. SM2 focuses on the convergence of the inner DMFT loop. This inner cycle represents the iterative solution of the quantum impurity problem.

In this stage the local lattice Green's function obtained from the DFT electronic structure is used to construct the hybridization function of the impurity model. The impurity solver then produces a correlated self-energy $\Sigma(\omega)$, which is fed back into the lattice Green's function and the DMFT equations. This procedure is repeated until the impurity Green's function and the self-energy become internally consistent. Importantly, the calculation proceeds to the next step of the outer DFT+DMFT cycle only after this inner DMFT loop has reached convergence.

Figure SM2 shows the evolution of μ [panels (a–c)] and the relative total energy $E_{tot} - E_0$ [panels (d–f)] as a function of the inner DMFT iteration number during the final outer cycle ($N = 12$), where E_0 corresponds to the converged total energy of this outer iteration. In contrast to the slower convergence of the global charge–self–consistent loop, the quantities in the inner DMFT iteration stabilize rapidly after only a few iterations.

This rapid stabilization demonstrates that the impurity self-energy and the lattice Green's function reach mutual consistency within only a few iterations once the lattice charge density is fixed. Consequently, the slower conver-

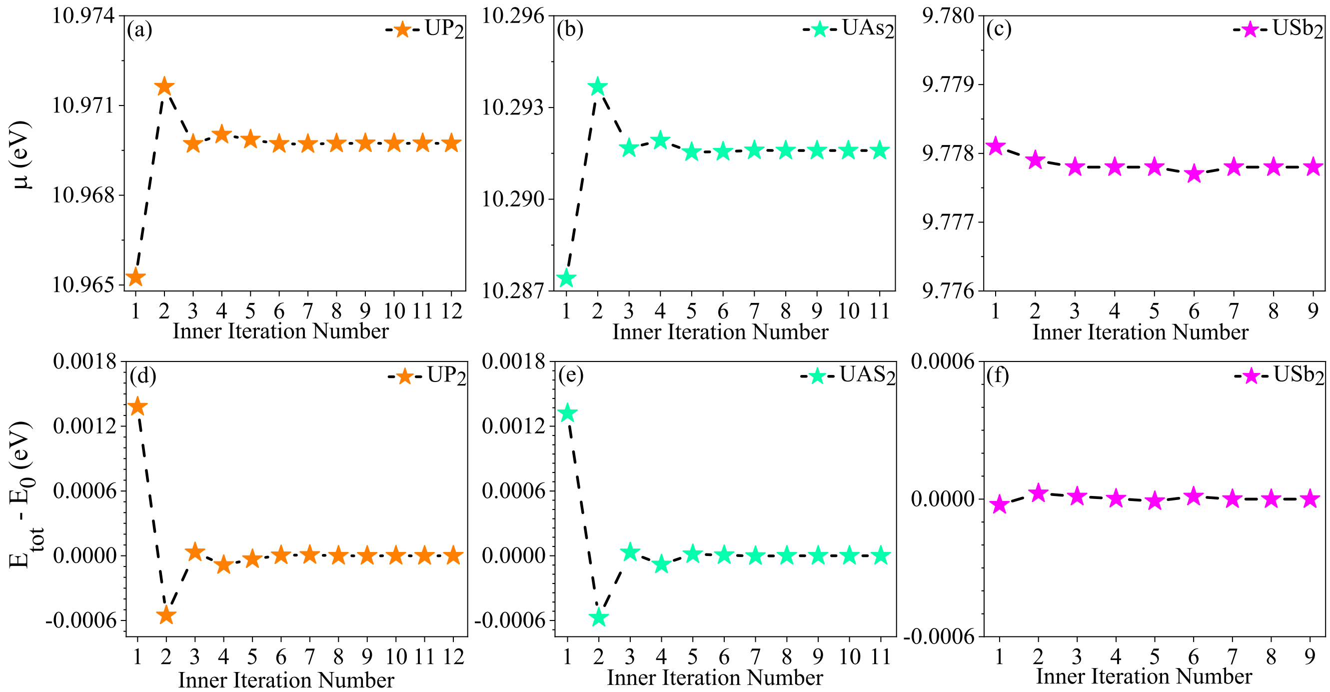

FIG. SM2. Convergence of the inner (embedded) DMFT impurity loop within the outer charge–self–consistent DFT+DMFT cycle including SOC at zero pressure for UP_2, UAs_2, and USb_2. The results are evaluated during the final outer iteration ($N = 12$). The chemical potential μ and the relative total energy $E_{\rm tot} - E_0$ are plotted as functions of the *inner* DMFT iteration number, where E_0 denotes the converged total energy of the final outer iteration. Panels (a–c) show the evolution of μ for UP_2, UAs_2, and USb_2, respectively, while panels (d–f) display the corresponding relative energies $E_{\rm tot} - E_0$, demonstrating the rapid stabilization of the inner DMFT loop.

gence observed in Fig. SM1 is governed primarily by the global charge–self–consistent cycle rather than by the impurity solver itself.

Taken together, Figs. SM1 and SM2 illustrate the two complementary levels of convergence in the DFT+DMFT framework: the slower convergence of the outer charge–self–consistent electronic structure and the much faster convergence of the inner DMFT impurity problem embedded within each outer iteration.

SMIV. CONVERGENCE AND VALIDATION

The convergence behavior of the outer charge–self–consistent DFT+DMFT cycle and the inner DMFT impurity loop is illustrated in the previous sections. In the present calculations, the outer loop was considered converged when the change in total charge between successive iterations was smaller than 10^{-4} e per formula unit and the total energy variation was below 10^{-5} Ry.

Within each outer iteration, the impurity problem was solved self–consistently until the change in impurity occupancy between successive inner iterations was less than 10^{-3} and the Matsubara Green's functions and self–energies became stable within the statistical accuracy of the solver. These criteria ensure that both the Kohn–Sham charge density and the DMFT self–energy are numerically converged.

Additional consistency checks were performed to verify the stability of the projector construction and the embedding procedure. These tests confirmed that the calculated electronic and magnetic properties are robust with respect to small numerical variations, ensuring the reliability of the reported results.

SMV. HYBRIDIZATION-FUNCTION CONSTRUCTION AND SOLVER-INPUT WORKFLOW

To clarify the provenance, matrix structure, reduction, and computational use of the hybridization functions analyzed in Fig. 2, we summarize in Fig. SM3 the complete workflow connecting the DFT+DMFT output to the final CT-QMC impurity-solver input. This clarification is important because the quantity plotted in Fig. 2 is not the unreduced matrix-valued hybridization itself, but a symmetry-reduced channel quantity derived from it.

The starting point of the workflow is the DFT+DMFT stage, which generates the intermediate file `case.dlt1`. This file stores the Matsubara-frequency hybridization data in terms of independent complex components. In the correlated subspace, however, the hybridization function is matrix-valued, and its interpretation therefore requires structural information specifying how the independent components are organized.

This structural information is provided by `case.indmfl`, which defines the local correlated

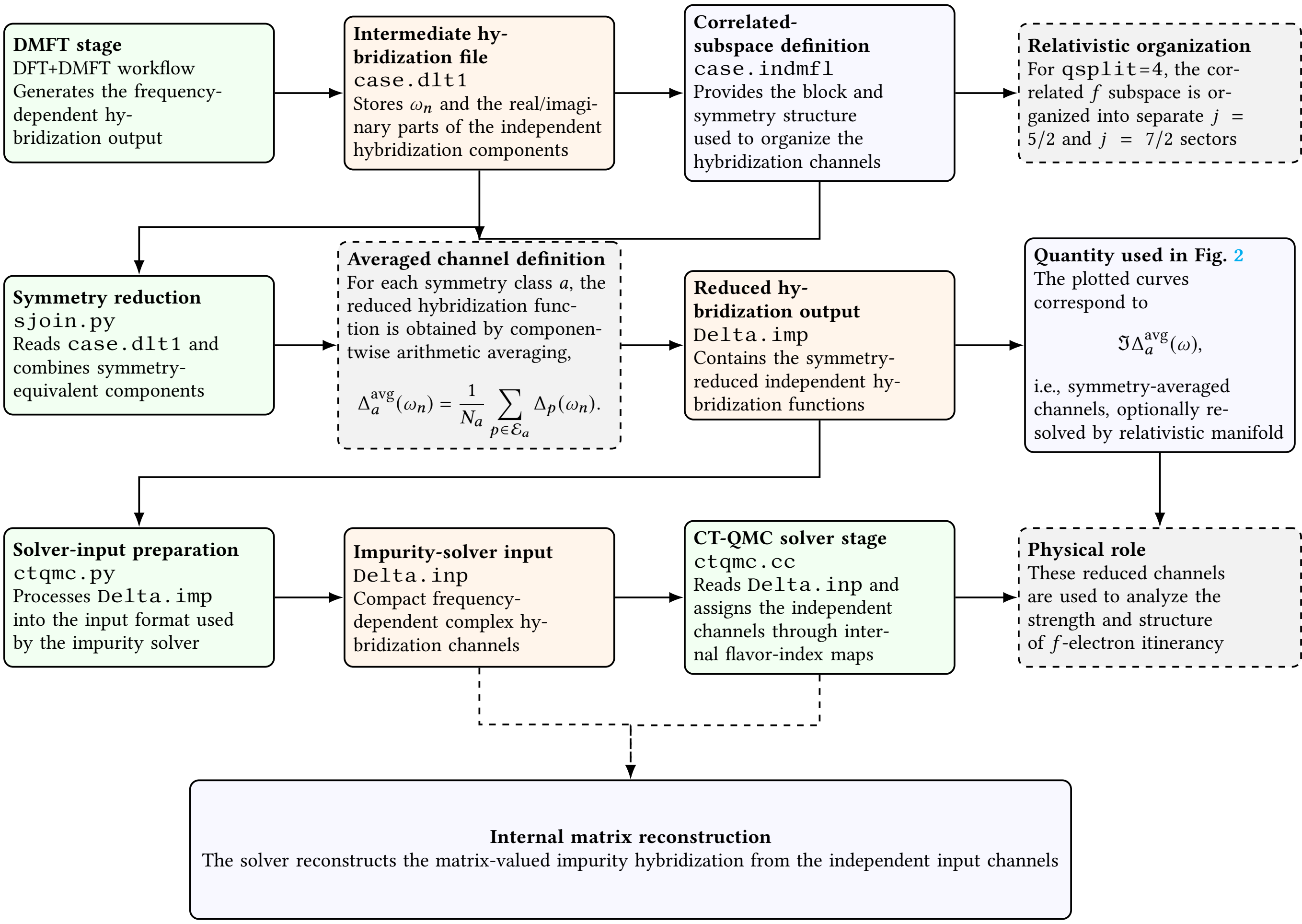

FIG. SM3. Workflow used to construct the hybridization functions discussed in Fig. 2. The DFT+DMFT stage generates the intermediate file `case.dlt1`, which stores Matsubara-frequency hybridization data in terms of independent complex components. The correlated subspace is defined by `case.indmfl`, which provides the block- and symmetry-resolved structure used in the reduction stage. The script `sjoin.py` reads `case.dlt1`, groups symmetry-equivalent components, and constructs reduced hybridization channels by componentwise arithmetic averaging, $\Delta_a^{\mathrm{avg}}(\omega_n) = \frac{1}{N_a}\sum_{p\in\mathcal{E}_a}\Delta_p(\omega_n)$. The resulting reduced channels are written to `Delta.imp`, then processed by `ctqmc.py` into the impurity-solver input file `Delta.inp`. In the CT-QMC solver, implemented in `ctqmc.cc`, these independent channels are assigned through internal flavor-index mappings and used to reconstruct the matrix-valued impurity hybridization. Accordingly, the curves shown in Fig. 2 represent the imaginary part of the symmetry-reduced hybridization function, $\Im\Delta_a^{\mathrm{avg}}(\omega)$, or, when presented in block-resolved form, the corresponding j-resolved channels. These plotted quantities are symmetry-reduced channel functions and should not, in general, be interpreted as the trace of the full hybridization matrix.

subspace together with its block and symmetry organization. In practical usage, this file is read and processed through the DMFT interface tools by constructing an `Indmfl` object and invoking its `read()` method. The internal organization of the correlated subspace is governed by the parameter `qsplit`, whose allowed conventions are documented in `indmffile.py`. In the present calculation, `case.indmfl` sets `qsplit=4` for the correlated uranium sites. In the `indmffile.py` convention, `qsplit=4` denotes the relativistic $|j, m_j\rangle$ representation, retaining the two spin-orbit split subspaces $j = l - 1/2$ and $j = l + 1/2$ as separate manifolds. For the uranium f shell, these correspond to the two total-angular-momentum sectors $j = l - \frac{1}{2} = 5/2$ and $j = l + \frac{1}{2} = 7/2$, which are explicitly identified as separate blocks in `case.indmfl`. Therefore, the independent hybridization data are organized in a form consistent with separate $j = 5/2$ and $j = 7/2$ channels, rather than as a single undifferentiated 14×14 object.

The next step is the symmetry reduction of the independent hybridization components. As implemented in `sjoin.py`, the code reads the hybridization file `case.dlt1` and writes the reduced output `Delta.imp`. In this step, symmetry-equivalent components are accumulated with multiplicity normalization, as seen explicitly from the update rules used for the real and imaginary parts. For a given symmetry class a, we therefore define the reduced hybridization channel as

$$\Delta_a^{\mathrm{avg}}(\omega_n) = \frac{1}{N_a} \sum_{p \in \mathcal{E}_a} \Delta_p(\omega_n), \tag{SM1}$$

where $\mathcal{E}_a$ denotes the set of independent components assigned to symmetry class a, and $N_a = |\mathcal{E}_a|$ is its multiplicity. Equation (SM1) is the explicit reduction by which the matrix-valued hybridization is converted into the channel-resolved quantity used for analysis.

The quantities displayed in Fig. 2 are based on these reduced channels. Specifically, the plotted curves correspond to

$$\Im \Delta_a^{\mathrm{avg}}(\omega), \tag{SM2}$$

or, equivalently, to manifold-resolved symmetry-averaged hybridization channels associated with a given relativistic sector. Thus, although $\Delta(\omega)$ is formally a matrix quantity, the data shown in Fig. 2 are channel-resolved quantities obtained from that matrix through the averaging operation in Eq. (SM1). In general, this symmetry-averaged channel is not identical to the normalized trace of the corresponding hybridization block; the two coincide only if the averaging set exhausts the complete set of diagonal components entering that block with equal weight. In this sense, Fig. 2 does not display the full $j = 5/2$ or $j = 7/2$ hybridization block directly, but rather the imaginary part of the corresponding symmetry-reduced channel derived from it.

This reduction step is physically motivated and not merely a graphical simplification. In a relativistic correlated-orbital problem, the raw hybridization output may contain several entries that are symmetry-equivalent but separately listed because of basis indexing and internal matrix representation. The averaging defined in Eq. (SM1) removes this redundancy and yields a compact set of channels that can be compared directly across different thermodynamic or structural conditions. The resulting reduced channels are written to `Delta.imp`, which therefore serves as the first analysis-oriented output of the workflow.

After the reduced hybridization channels have been constructed, the workflow proceeds to the solver-input preparation stage. The script `ctqmc.py` defines `Delta.inp` as the solver hybridization input and writes that file in the impurity-solver directory. This step is computationally important because the representation most suitable for analysis is not necessarily identical to the representation required by the solver. The file `Delta.imp` is convenient for symmetry-resolved interpretation, whereas `Delta.inp` is designed for efficient parsing and channel assignment within the impurity solver. The role of `ctqmc.py` is therefore to translate the reduced hybridization data from an analysis-oriented form into a solver-oriented form without changing their physical content.

The next stage is the CT-QMC solver itself, represented in Fig. SM3 by `ctqmc.cc`. This code reads the hybridization input and internally assigns the independent channels through flavor-index maps. In particular, the mappings `tfl_index` and `bfl_index` are explicitly defined and used to connect the independent bath channels to the matrix elements required in the impurity calculation. The solver therefore operates on a matrix-valued hybridization function even though the user-facing input is supplied in terms of reduced independent channels. These channels are thus not the final form in which the impurity problem is evaluated; rather, they are mapped internally into the orbital/flavor structure of the correlated subspace and used to reconstruct the matrix-valued impurity hybridization entering the many-body calculation.

From the perspective of reproducibility, the sequence

$$\begin{aligned}\texttt{case.dlt1} &\rightarrow \texttt{sjoin.py} \rightarrow \texttt{Delta.imp} \\ &\rightarrow \texttt{ctqmc.py} \rightarrow \texttt{Delta.inp} \\ &\rightarrow \texttt{ctqmc.cc}\end{aligned} \tag{SM3}$$

provides a transparent computational chain linking the DFT+DMFT output to the impurity-solver execution. In this chain, `case.dlt1` stores the raw frequency-dependent hybridization components; `sjoin.py` performs the symmetry reduction according to Eq. (SM1); `Delta.imp` stores the reduced channels; `ctqmc.py` reformats these channels into the solver-input file `Delta.inp`; and `ctqmc.cc` reads this compact input and reconstructs the matrix-valued hybridization internally.

The physical interpretation of Fig. 2 should therefore be understood in light of the complete workflow summarized above. The curves shown there are not unreduced matrix elements taken directly from `case.dlt1`; rather, they are symmetry-reduced, manifold-resolved hybridization channels obtained from the matrix-valued DFT+DMFT hybridization through Eq. (SM1), visualized through Eq. (SM2), and subsequently passed in compact form through the chain given in Eq. (SM3) to the CT-QMC solver, where they are reassembled into the matrix-valued hybridization used in the many-body treatment. Figure SM3 therefore serves not only as a technical flowchart, but also as a methodological bridge between the formal matrix-valued hybridization of the DMFT impurity problem and the reduced channel quantities used in Fig. 2 to analyze the strength and structure of f-electron itinerancy.

SMVI. COMPUTATIONAL WORKFLOW FOR PARAMAGNETIC LOCAL MOMENTS

As summarized schematically in Fig. SM4, the paramagnetic local moment is extracted from the DMFT impurity solution in a fully reproducible, operator-based manner. The central quantity is the longitudinal local-moment operator

$$\hat{m}_z = -\mu_B(\hat{L}_z + 2\hat{S}_z), \tag{SM4}$$

whose fluctuations are evaluated from the impurity density matrix generated by the CT-QMC solver. In the workflow shown in Fig. SM4, the impurity problem is defined by the hybridization function $\Delta_k(i\omega_n)$. As specified in Eq. (SM2) and illustrated in Fig. 2, this function accounts for the relativistic $j = 5/2$ ($k = 1$) and $j = 7/2$ ($k = 2$) sectors, with the

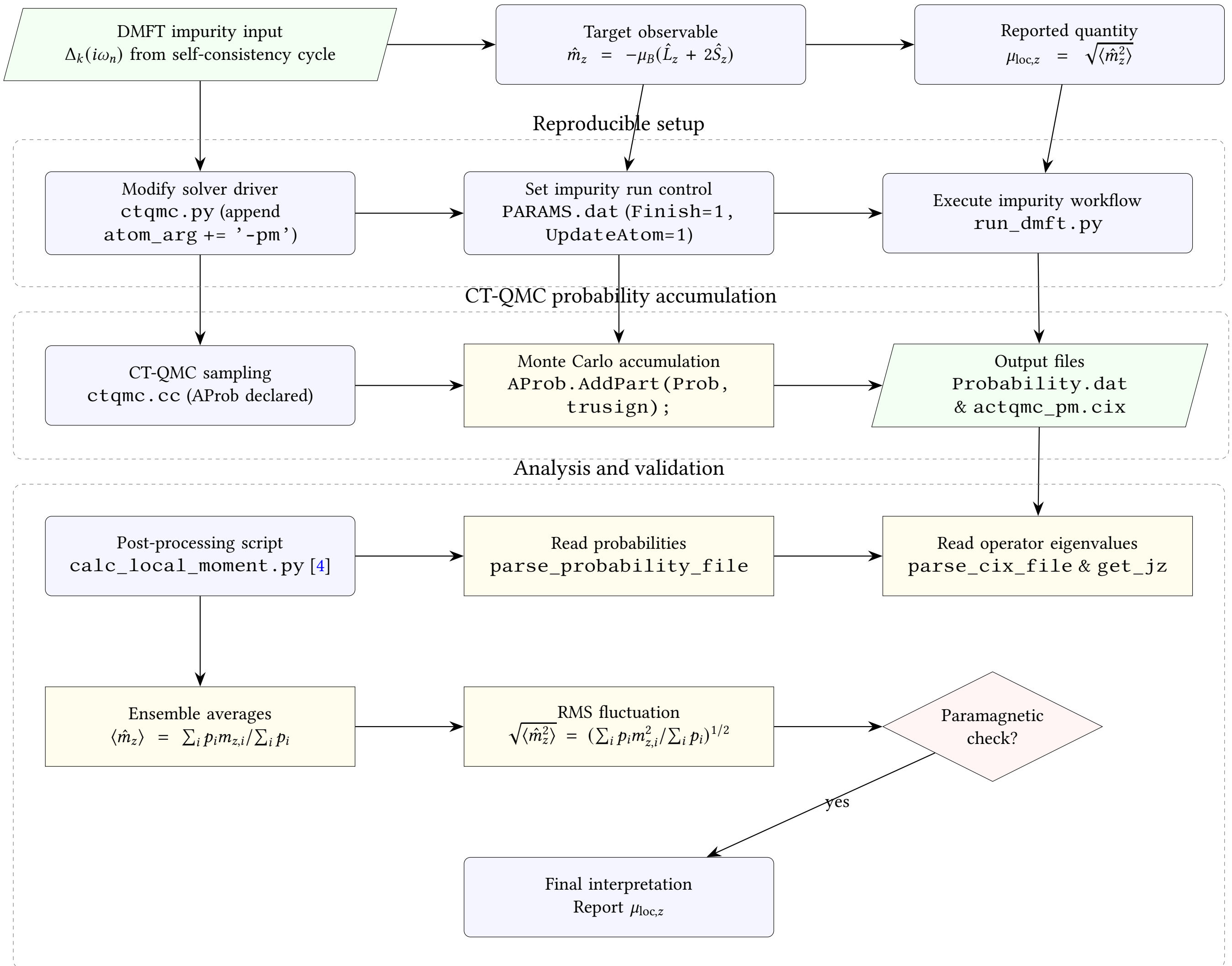

FIG. SM4. Flowchart of the reproducible evaluation of the paramagnetic local moment from the DMFT impurity calculation. The procedure starts from the Matsubara-frequency hybridization input, activates paramagnetic operator-based sampling in the impurity solver, accumulates impurity-state probabilities internally through `AProb`, writes the averaged probability distribution to `Probability.dat`, and finally combines these probabilities with the longitudinal operator eigenvalues extracted from the impurity basis file to compute $\langle \hat{m}_z \rangle$, $\langle |\hat{m}_z| \rangle$, and $\sqrt{\langle \hat{m}_z^2 \rangle}$. The latter is reported as the paramagnetic local moment $\mu_{\mathrm{loc},z}$.

corresponding symmetry-index reduction and hybridization usage illustrated in Fig. SM3. This function enters as discrete Matsubara-frequency input from the DMFT self-consistency cycle, thereby determining the dynamical environment sampled by the impurity solver.

The paramagnetic local moment reported in Table I of the main manuscript is defined, as indicated in Fig. SM4, by the root-mean-square fluctuation of the longitudinal operator,

$$\mu_{\mathrm{loc},z} = \sqrt{\langle \hat{m}_z^2 \rangle}, \tag{SM5}$$

where $\langle \ldots \rangle$ denotes the impurity-ensemble expectation value obtained from CT-QMC sampling, see Sec. IV A of the main text. As emphasized by the flowchart in Fig. SM4, this definition avoids isolated-atom moment formulas and instead evaluates the fluctuating moment directly from the embedded impurity states.

To reproduce the operator-based sampling mode highlighted in Fig. SM4, the impurity-solver driver `ctqmc.py` must be modified so that the atomic-solver argument string `atom_arg` includes the paramagnetic flag

```
atom_arg += ' -pm '
```

This step, shown in the upper-left branch of Fig. SM4, activates sampling of longitudinal magnetic fluctuations in the impurity ensemble.

The corresponding impurity execution path is also given in Fig. SM4. In the parameter file `PARAMS.dat`, the flags

```
Finish = 1
UpdateAtom = 1
```

are used to enforce a single-cycle impurity run with updated atomic information. The workflow is then executed through

```
run_dmft.py
```

which, as shown in Fig. SM4, generates the converged impurity-state probability distribution used in the moment analysis.

The CT-QMC solver accumulates the statistical information internally through the object `AProb`, which is explicitly indicated in Fig. SM4. This object is declared in `ctqmc.cc` and initialized to zero. During Monte Carlo sampling, the instantaneous probability distribution `Prob` is accumulated via

```
AProb.AddPart(Prob, trusign);
```

as shown in the internal accumulation stage of Fig. SM4. After convergence, the averaged probabilities are written to `Probability.dat`, which is the output file used in the post-processing branch of Fig. SM4.

The final moment analysis, shown in the lower half of Fig. SM4, is performed by `calc_local_moment.py` [4]. The function `parse_probability_file` reads the probability weights p_i from `Probability.dat`, while `parse_cix_file` extracts the corresponding operator eigenvalues from the impurity basis file. Although the implementation labels these quantities as J_z, Fig. SM4 shows that they are used operationally as the longitudinal magnetic eigenvalues entering Eq. (SM5). In the distributed source code, the quantity J_z is accessed through `Jz(int state)` in `atomh.cc`, defined as `double Jz(int state) const { return Lz(state)+Sz(state);}`. The conversion between J_z values and internal integer indices is implemented by `give_iJz(double Jz)` and `give_Jz(int iJz)` in the same file.

Consistent with the analysis block in Fig. SM4, the ensemble averages are computed as

$$\langle \hat{m}_z \rangle = \frac{\sum_i p_i m_{z,i}}{\sum_i p_i}, \tag{SM6}$$

$$\langle |\hat{m}_z| \rangle = \frac{\sum_i p_i |m_{z,i}|}{\sum_i p_i}, \tag{SM7}$$

and

$$\sqrt{\langle \hat{m}_z^2 \rangle} = \left(\frac{\sum_i p_i m_{z,i}^2}{\sum_i p_i} \right)^{1/2}, \tag{SM8}$$

where $m_{z,i}$ is the longitudinal eigenvalue associated with impurity state i. As indicated in Fig. SM4, these quantities are the direct outputs of the probability-weighted evaluation.

Reproducibility of the full procedure is obtained by running

```
python3 calc_local_moment.py
actqmc_pm.cix Probability.dat
```

in the directory containing the converged DMFT outputs, exactly as represented in the lower workflow block of Fig. SM4.

The validation criteria shown at the bottom of Fig. SM4 are then applied. The probability distribution satisfies $\sum_i p_i = 1$ within numerical precision. In the paramagnetic regime, $\langle \hat{m}_z \rangle \approx 0$, consistent with the absence of static symmetry breaking, whereas $\langle |\hat{m}_z| \rangle$ and $\sqrt{\langle \hat{m}_z^2 \rangle}$ remain finite, demonstrating genuine dynamical local-moment fluctuations. Accordingly, the paramagnetic local moment reported in this work is identified with the RMS quantity in Eq. (SM8), matching the final interpretation block of Fig. SM4 and providing a direct operator-based measure extracted from the DMFT impurity density matrix.

SMVII. ELECTRONIC STRUCTURE OF UP_2 IN THE EXPERIMENTALLY ESTABLISHED *I4/MMM* PHASE

Early studies of the uranium dipnictides UX_2 reported that these compounds crystallize in the tetragonal anti–Cu_2Sb (PbFCl)–type structure with space group $P4/nmm$ [1, 2]. In this structural description all uranium atoms are crystallographically equivalent and the pnictogen atoms occupy two inequivalent sites, leading to a layered tetragonal framework that naturally promotes strong electronic anisotropy [1, 2].

Subsequent high-resolution single-crystal x-ray diffraction measurements by Wiśniewski *et al.* [3] revealed that UP_2 does not crystallize in the simple anti–Cu_2Sb–type structure originally proposed for the uranium dipnictide series. Instead, it adopts a more complex tetragonal structure with space group $I4/mmm$. In the present work, however, we employ the $P4/nmm$ structure as a common crystallographic reference for the UX_2 series in order to analyze correlation-driven trends on an equal structural footing.

Subsequent high-resolution single-crystal x-ray diffraction measurements by Wiśniewski *et al.* [3] revealed that UP_2 adopts a more complex tetragonal structure with space group $I4/mmm$, rather than the simpler anti–Cu_2Sb–type structure originally proposed for the uranium dipnictide series. This refined crystallography is characterized by enlarged lattice parameters and, importantly, by the presence of three crystallographically inequivalent uranium sites. The breaking of uranium site equivalence introduces subtle variations in the local $5f$ coordination environments and in the hybridization pathways with surrounding ligand p orbitals. Despite these distinctions, the overall diffraction signatures of the $I4/mmm$ and anti–Cu_2Sb ($P4/nmm$) structures are remarkably similar because the fundamental stacking sequence of uranium and pnictogen layers and their local coordination geometries remain essentially related.

Owing to this close structural resemblance, and for the sake of cross-comparative analysis, many experimental and theoretical works have continued to employ the simpler $P4/nmm$ structural description even after the refinement of Wiśniewski *et al.* For example, Tsutsui *et al.* [5] analyzed ^{238}U Mössbauer spectra and extracted electric-field gradients (EFGs) across the UX_2 series within the $P4/nmm$ crystallographic framework, explicitly noting that UP_2 had later been reassigned to the $I4/mmm$ space group but that the calculated diffraction intensities and hyperfine parameters ob-

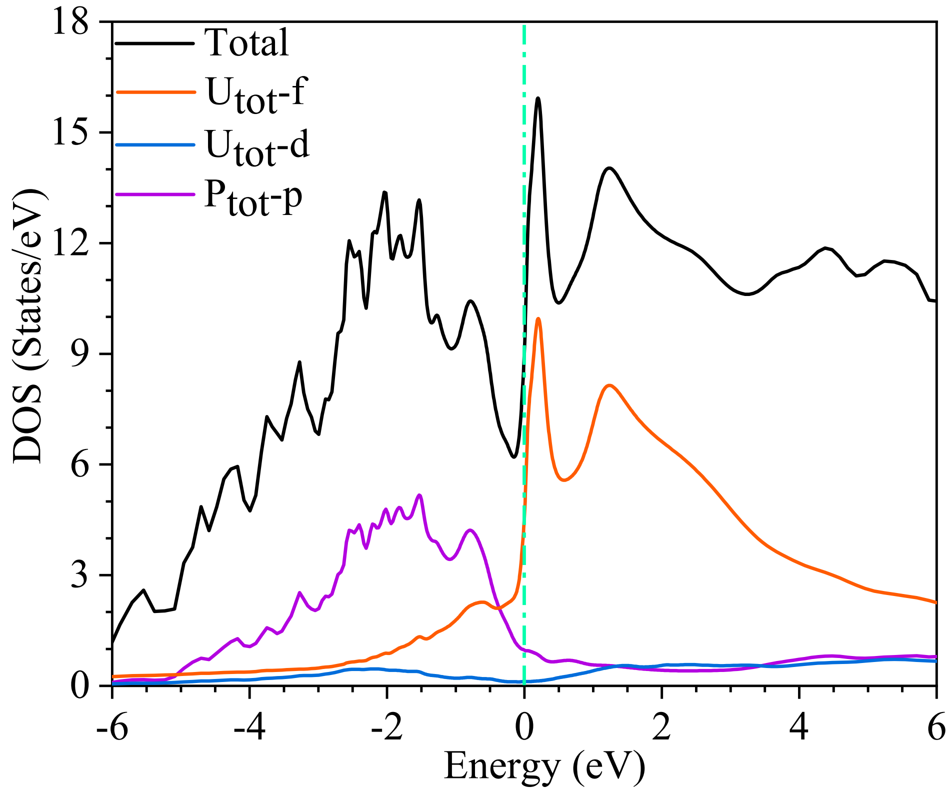

FIG. SM5. Total and atomic-orbital-resolved densities of states (DOS) for UP_2 in the tetragonal $I4/mmm$ structure at zero pressure. The vertical dashed–dotted lines denote the Fermi level. All results are obtained from fully charge-self-consistent DFT+DMFT calculations including SOC.

tained within either description were nearly indistinguishable. This pragmatic choice has led to widespread use of the $P4/nmm$ model as a unified structural reference for uranium dipnictides, allowing correlation–driven and chemical trends to be isolated from purely structural effects.

First-principles studies have largely followed this convention. In particular, our previous hybrid-functional investigation [6] reproduced the experimentally observed evolution of EFGs across the UX_2 (X = P, As, Sb, Bi) series using the $P4/nmm$ structure. That work obtained finite EFG values for UP_2, UAs_2, and USb_2 and an almost negligible one for UBi_2, fully consistent with the nuclear quadrupole resonance data reported by Tsutsui *et al.* [5]. The analysis demonstrated that the striking contrast in EFG magnitude within the series primarily reflects differences in magnetic ordering, rather than lattice distortions or changes in the degree of f–p hybridization.

More recent first-principles investigations of structural stability, elastic coefficients, and thermodynamic properties in UX_2 compounds have also adopted the anti–Cu_2Sb framework as a consistent reference model to facilitate systematic comparisons across different ligand species [7]. In a similar vein, symmetry-based tabulations of magnetic materials, such as Table I of the Supplementary Material of Ref. [8], likewise classify UP_2 under the tetragonal $P4/nmm$ group to maintain uniformity within the broader UX_2 family.

For these reasons, the main paper—apart from Appendix B, where the experimentally refined structure is explicitly analyzed—uses the $P4/nmm$ structure as a unified crystallographic platform to characterize the correlation-driven and chemical trends across the UX_2 series without introducing additional structural variables. Nevertheless, it is important to emphasize that the experimentally established ground-state structure of UP_2 is indeed tetragonal $I4/mmm$, featuring three nonequivalent uranium sublattices with distinct local coordination environments around each U site [3].

To quantitatively assess the influence of this structural refinement on the correlated uranium $5f$ electronic states, we have therefore recalculated the full electronic structure of UP_2 within its experimentally determined $I4/mmm$ phase using the same fully charge–self–consistent DFT+DMFT framework described in Sec. II of the main paper. The following subappendices present a detailed analysis of the correlated electronic structure, spectral functions, and thermodynamic diagnostics of UP_2 in the $I4/mmm$ structure, and they provide a direct one-to-one comparison with the results obtained for the $P4/nmm$ reference configuration.

SM I. Spin–Orbit–Resolved DOS and Pressure-Tuned Hybridization

Figure SM5 [Fig. B1(a_1) of the main paper] presents the total and orbital-resolved densities of states (DOS) of UP_2 in its experimentally reported tetragonal $I4/mmm$ structure at zero pressure, obtained from fully charge-self-consistent DFT+DMFT calculations including spin–orbit coupling. The spectral decomposition offers a microscopic view of the contributions from different atomic orbitals and reveals the characteristic features that govern the correlated metallic nature of this phase.

The most pronounced peak in the vicinity of the Fermi level (E_F), marked by the vertical dashed-dotted line in Fig. SM5, originates predominantly from uranium $5f$ states. The presence of a sharp quasiparticle resonance around E_F indicates the formation of coherent many-body excitations from strongly correlated $5f$ electrons. This feature signifies that the $5f$ electrons are neither fully localized nor completely itinerant, but rather participate in partially itinerant quasiparticle states where electronic correlations lead to substantial renormalization of the spectral weight. The low-energy part of the spectrum is therefore governed by the uranium $5f$ manifold, whose correlated nature defines the intrinsic metallic character of UP_2.

Outside the immediate neighborhood of the Fermi energy, the DOS is dominated by ligand-derived states. The phosphorus $3p$ orbitals occupy the valence region predominantly between -6 and approximately -0.5 eV, forming broad dispersive bands that represent typical ligand-p behavior. Their spectral weight diminishes sharply as the energy approaches E_F, yet a weak tail of $3p$ character remains near the Fermi level, illustrating finite hybridization with uranium $5f$ orbitals. This hybridization channel plays a critical role in mediating the partial itinerancy of the correlated $5f$ electrons. Meanwhile, the uranium $6d$ states contribute only modestly throughout the studied energy range and do not exhibit distinct features near E_F, underscoring their secondary role in shaping the low-energy electronic structure.

Above the Fermi level, the conduction region is characterized by relatively broad spectral weight extending over several electronvolts. In this energy range the DOS reflects contributions from uranium-derived states, including $5f$ and $6d$ components, together with residual phosphorus $3p$ character. Compared with the sharp quasiparticle feature at E_F, the spectral weight above the Fermi level is more extended and less structured, indicating more dispersive electronic states that participate in the unoccupied conduction bands. The coexistence of uranium and ligand character in this region reflects continued f–p hybridization beyond the immediate vicinity of the Fermi level, which facilitates charge fluctuations between uranium and the surrounding phosphorus environment. Such hybridized conduction states therefore provide an important channel for the partial delocalization of the correlated $5f$ electrons.

These observations reveal a clear orbital hierarchy in UP_2: the low-energy excitations are dominated by uranium $5f$ states, while the deeper valence region is primarily composed of phosphorus $3p$ orbitals.

Establishing this global orbital distribution is essential for interpreting the finer internal structure of the $5f$ manifold itself. In particular, once spin–orbit coupling is explicitly resolved, the uranium $5f$ states split into distinct total-angular-momentum multiplets whose spectral weights distribute differently across the low-energy region. The next panel therefore focuses on resolving the $5f$ spectral weight into its spin–orbit–split $j = 5/2$ and $j = 7/2$ components to clarify which manifold primarily governs the quasiparticle states near the Fermi level and how the correlated $5f$ electrons organize within the spin–orbit-coupled electronic structure of UP_2.

Figure SM6 [Fig. B1(a_2) of the main paper] directly builds upon the well-established global orbital hierarchy depicted in Fig. SM5 by explicitly resolving the uranium $5f$ spectral weight into its spin–orbit–coupled components. In actinide systems such as UP_2, the strong atomic spin–orbit interaction dramatically lifts the degeneracy of the $5f$ shell, resulting in well-separated $j = 5/2$ and $j = 7/2$ manifolds. The relative positioning and spectral distribution of these manifolds are crucial in dictating the degree of f electron itinerancy, their hybridization with ligand states, and the nature of the many-body low-energy excitations.

In this case, the DMFT spectral function exhibits stark separation: the $j = 5/2$ states form a narrow, coherent quasiparticle peak sharply pinned at the Fermi level, indicating the presence of strongly renormalized, partially itinerant f electrons that govern the metallic behavior of UP_2. Conversely, the $j = 7/2$ manifold is predominantly situated above the Fermi energy, extending into the unoccupied spectral region, and displays a broad, incoherent profile. The inset magnifies the $j = 5/2$ resonance, revealing an asymmetric, narrow peak characteristic of mass renormalization and coherent low-energy quasiparticles.

This pronounced dominance of the $j = 5/2$ states at E_F demonstrates that the low-energy excitations responsible for the metallic properties originate almost exclusively within this manifold. Despite the considerable spectral weight of the higher $j = 7/2$ states, these occupy a largely unoccupied, higher-energy region, reflecting the internal redistribution of $5f$ spectral weight driven by strong spin–orbit coupling combined with electron-electron correlations. Such a splitting is a hallmark of uranium-based heavy-fermion and mixed-valence compounds, where the subtle interplay between SOC and correlations critically shapes the emergence of quasiparticles, hybridization effects, and valence fluctuations.

Furthermore, the clear separation between the $j = 5/2$ and $j = 7/2$ manifolds provides a valuable foundation for future investigations: it enables us to analyze how external parameters—pressure, hybridization strength, or lattice distortions—may selectively modify these channels and influence the building blocks of the low-energy physics. This

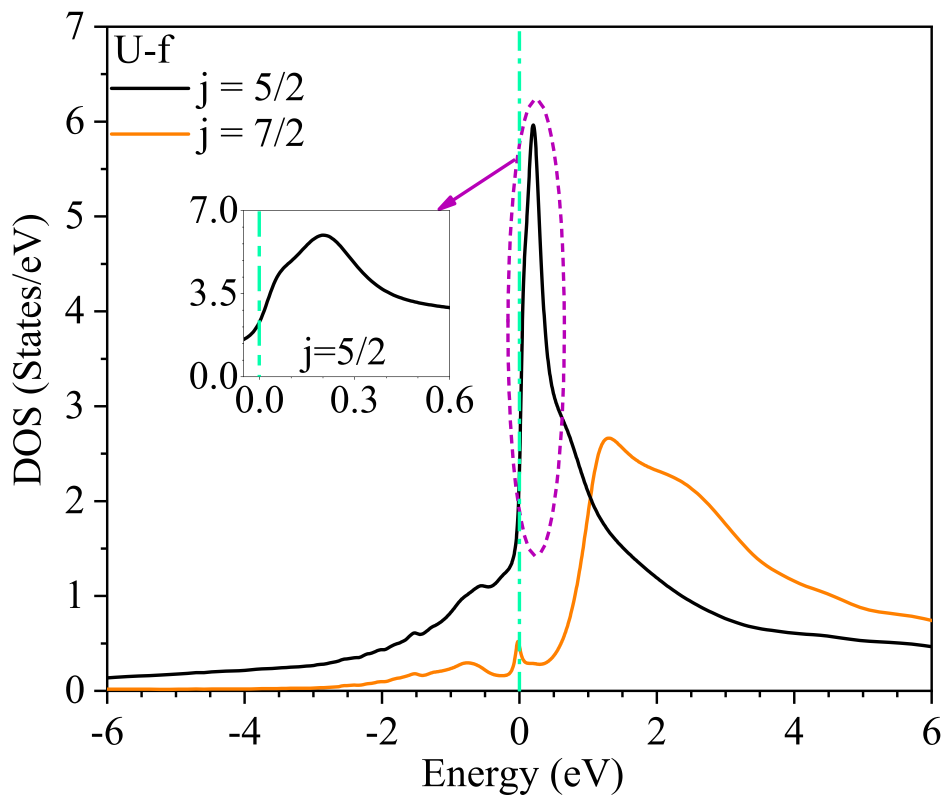

FIG. SM6. Spin–orbit–coupling (SOC) resolved U $5f$ states, illustrating the splitting into $j = 5/2$ and $j = 7/2$ manifolds for UP_2 in the tetragonal $I4/mmm$ structure at zero pressure. The vertical dashed–dotted lines denote the Fermi level. All results are obtained from fully charge-self-consistent DFT+DMFT calculations using PBE–GGA and including SOC.

sets a crucial stage for understanding how such microscopic changes translate into macroscopic phenomena, including hybridization gaps, mass enhancement, or potential magnetic/spin–orbit-driven phase transitions.

Finally, this internal spin–orbit-resolved structure of the $5f$ manifold prepares us for subsequent analyses of the SOC effects in the full electronic structure, emphasizing the importance of the $j = 5/2$ states in the emergent correlated metallic state of UP_2, and how they evolve under external perturbations.

Figure SM7 [Fig. B1(a_3) of the main paper] illustrates the response of the correlated electronic structure of UP_2 to hydrostatic compression by comparing the total density of states at ambient pressure with that obtained at $P = 4.427$ GPa. Because pressure primarily reduces interatomic separations, it modifies the overlap between uranium and ligand orbitals and thus directly influences the hybridization processes that control the itinerancy of the $5f$ electrons. The comparison therefore provides a direct view of how the correlated spectral landscape reorganizes when the lattice is compressed.

Globally, the overall structure of the DOS remains largely preserved under pressure. The broad valence region extending from approximately −6 to −1 eV shows only modest changes, indicating that the deeper ligand-dominated states remain relatively insensitive to the moderate compression considered here. The most visible differences emerge in the vicinity of the Fermi level, where the correlated f-derived quasiparticle structure resides. In both pressure conditions the system maintains a finite density of states at E_F, confirming that UP_2 remains metallic. However, the detailed spectral profile around the Fermi level undergoes measurable modifications that reflect subtle changes in quasiparticle coherence and hybridization strength.

The most pronounced evolution occurs in the narrow spectral feature just above the Fermi energy, highlighted by the dashed ellipse in Fig. SM7. Under compression, this peak becomes sharper and its maximum increases significantly in intensity. At the same time, the shallow dip located almost exactly at E_F becomes slightly deeper. The inset, which zooms into the energy window between −0.5 and 0.5 eV, clearly resolves these changes: the near-E_F peak grows more pronounced and shifts marginally in energy, while the spectral weight immediately at the Fermi level is redistributed.

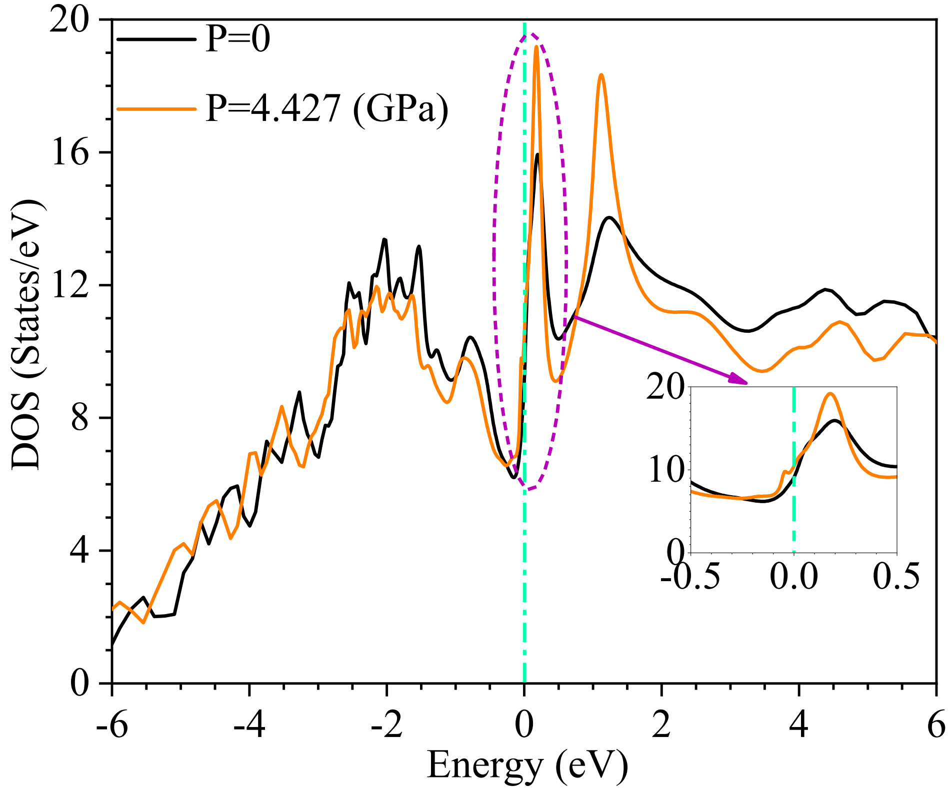

FIG. SM7. Comparison of the total DOS at ambient pressure (black) and under hydrostatic compression $P = 4.427$ GPa (orange), highlighting the evolution of electronic states near the Fermi energy for UP_2 in the tetragonal $I4/mmm$ structure. The vertical dashed–dotted lines denote the Fermi level. All results are obtained from fully charge-self-consistent DFT+DMFT calculations using PBE–GGA and including SOC.

This behavior indicates that pressure modifies the balance between coherent quasiparticle states and the surrounding background of broader excitations.

From a microscopic perspective, these changes are consistent with an increase in hybridization strength induced by lattice compression. As the U–P distances decrease, the overlap between uranium $5f$ orbitals and phosphorus-derived states becomes stronger, enhancing the effective hybridization channels that couple localized and itinerant electronic degrees of freedom. Within the DFT+DMFT framework, such enhanced hybridization typically promotes greater quasiparticle coherence by broadening the correlated bands and redistributing spectral weight toward low-energy excitations. The sharpening of the peak just above E_F can therefore be interpreted as an indication that the correlated quasiparticle states become slightly more coherent under pressure.

The pressure dependence also affects the unoccupied conduction region. Above the Fermi level, the spectral structure between roughly 0.5 and 2 eV exhibits noticeable reshaping: the dominant peak in this region shifts and becomes more intense under compression. This indicates that pressure modifies the distribution of available conduction states, likely reflecting changes in the hybridized uranium-derived bands that form the low-energy conduction manifold. Such modifications influence the phase space available for electronic excitations and charge fluctuations, which are essential ingredients of the mixed-valence physics discussed in the main text.

Despite these spectral rearrangements, the overall magnitude of the changes remains moderate. The correlated electronic structure retains the same qualitative form across the two pressures, indicating that the $5f$ electrons in UP_2 already occupy an intermediate regime between localized and itinerant limits at ambient conditions. Rather than inducing a drastic electronic reconstruction, hydrostatic compression gradually reinforces the hybridized metallic state by subtly increasing quasiparticle coherence and modifying the low-energy conduction spectrum.

Importantly, this pressure evolution is consistent with the spin–orbit-resolved picture discussed in Fig. SM6, where the quasiparticles near the Fermi level were shown to originate predominantly from the $j = 5/2$ component of the uranium $5f$ manifold. The enhanced sharpness of the near-E_F structure therefore likely reflects pressure-driven changes in the coherence and hybridization of these $j = 5/2$-derived states.

While the total DOS provides a global view of the pressure response, it does not yet reveal which orbital channels are primarily responsible for the observed spectral redistribution. To clarify the microscopic origin of these changes, the following analysis resolves the DOS into its orbital contributions, allowing us to track how the ligand p states and their hybridization with uranium $5f$ orbitals evolve under compression in UP_2.

To elucidate the microscopic mechanism underlying the pressure-induced spectral evolution seen in the total DOS (Fig. SM7), Fig. SM8 [Fig. B1(a_4) of the main paper] presents the pressure-dependent projected density of states for the phosphorus p orbitals. These ligand p states play a crucial role in shaping the hybridization landscape of UP_2: the correlated uranium $5f$ electrons responsible for the metallic behavior couple strongly to these extended ligand bands, which act as the conduction bath in the DMFT description. Examining how these ligand-derived states evolve under compression thus gives direct insight into how the hybridization environment and screening processes surrounding the $5f$ shell change with pressure.

At ambient pressure, the phosphorus p states form a broad composite valence band spanning approximately from −6 eV up to about −0.5 eV. The spectral intensity increases steadily from the deep valence region and reaches a pronounced maximum near −2 eV, corresponding to strongly bonding p states within the U–P network. This peak represents the main ligand-derived contribution to the occupied bandwidth and reflects substantial covalent interaction within the framework. The p spectral weight declines steeply as the Fermi level is approached, leaving only a weak tail extending toward E_F. This diminishing weight emphasizes that, at ambient pressure, the p orbitals act primarily as a hybridization partner for the uranium $5f$ states rather than as an active participant in low-energy metallic conduction.

Under hydrostatic pressure ($P = 4.427$ GPa), the general shape of the p-projected DOS remains qualitatively intact, revealing the robustness of the ligand electronic backbone against moderate lattice compression. However, several subtle quantitative modifications carry relevant physical meaning. First, the overall valence band broadens slightly, with its spectral features becoming smoother and extending further toward lower energy. This band broadening indicates enhanced inter-site orbital overlap—an expected consequence of reduced bond lengths—which increases the bandwidth of the ligand states. Second, the region between −3 and −1 eV, where the phosphorus p orbitals overlap with the hybridization tails of uranium $5f$ states, displays a notable redistribution of spectral intensity. The corresponding enhancement in spectral weight under pressure implies increased orbital mixing between p and f channels.

Most importantly, a faint but distinct increase in ligand spectral weight can be observed in the near-Fermi energy region. While the overall p contribution at E_F remains small, its subtle strengthening under pressure signals a more effective p–f mixing. This effect reflects an enhanced hybridization function in DMFT terms—pressure leads to stronger coupling between the correlated uranium impurity problem and its surrounding bath of ligand-derived conduction states. The increase of hybridization strength directly supports the emergence of sharper, more coherent quasiparticle resonance at E_F observed in Fig. SM7. The ligand p orbitals, therefore, serve as a sensitive probe of how structural compression promotes itinerancy: pressure amplifies their electronic participation in forming the conduction channel that stabilizes coherent $5f$ quasiparticles.

Beyond the low-energy regime, the pressure also subtly reshapes the unoccupied side of the spectrum, introducing a slight extension of p weight above the Fermi level. This reflects a shift in hybridization balance where ligand states begin to overlap more effectively with higher-energy $5f$ conduction bands, expanding the energy range of p–f coupling. Consequently, the hybridization matrix that links uranium and phosphorus orbitals becomes more delocalized, enabling smoother charge transfer and promoting metallic coherence.

Overall, these results reveal that the pressure response of UP_2 is driven not by isolated changes in the uranium $5f$ manifold, but by a cooperative evolution of both correlated and ligand subspaces. The phosphorus p orbitals act as an electronic bridge: they modulate the bandwidth and coherence of the $5f$ states by adjusting the degree of hybridization and charge transfer under compression. Even a relatively moderate pressure thus fine-tunes the delicate balance between localized f character and itinerant hybridized conduction, reinforcing the system's intermediate-valence nature.

Rather than turning immediately to the internal restructuring of the uranium $5f$ manifold, it is instructive to examine first how the broader uranium-derived electronic environment responds to compression. In particular, the uranium d orbitals occupy an intermediate position between the extended ligand p states and the highly correlated $5f$ shell. Their pressure dependence offers a valuable perspective on how the overall hybridization framework surrounding the $5f$ electrons is modified. By analyzing the U d-projected DOS, we can assess how changes in orbital overlap, bandwidth, and hybridization pathways propagate through the uranium electronic channels before isolating the specific many-body effects within the $5f$ sector itself.

Figure SM9 [Fig. B1(b_1) of the main paper] examines the pressure dependence of the uranium d-orbital spectral weight, providing an additional perspective on how the electronic environment surrounding the correlated $5f$ shell evolves under compression. Although the low-energy physics of UP_2 is dominated by the uranium $5f$ manifold, the more extended $6d$ orbitals form an important part of the broader hybridization network. Because of their larger spatial extent, these orbitals act as an intermediate channel that mediates coupling between the localized $5f$ electrons and the surrounding ligand p states. Tracking their spectral evolution therefore helps clarify how the uranium-centered conduction framework reorganizes as the lattice volume is reduced.

At ambient pressure, the U d-projected DOS exhibits a broad and relatively smooth distribution extending across the entire energy window from approximately −6 to 6 eV. The oc-

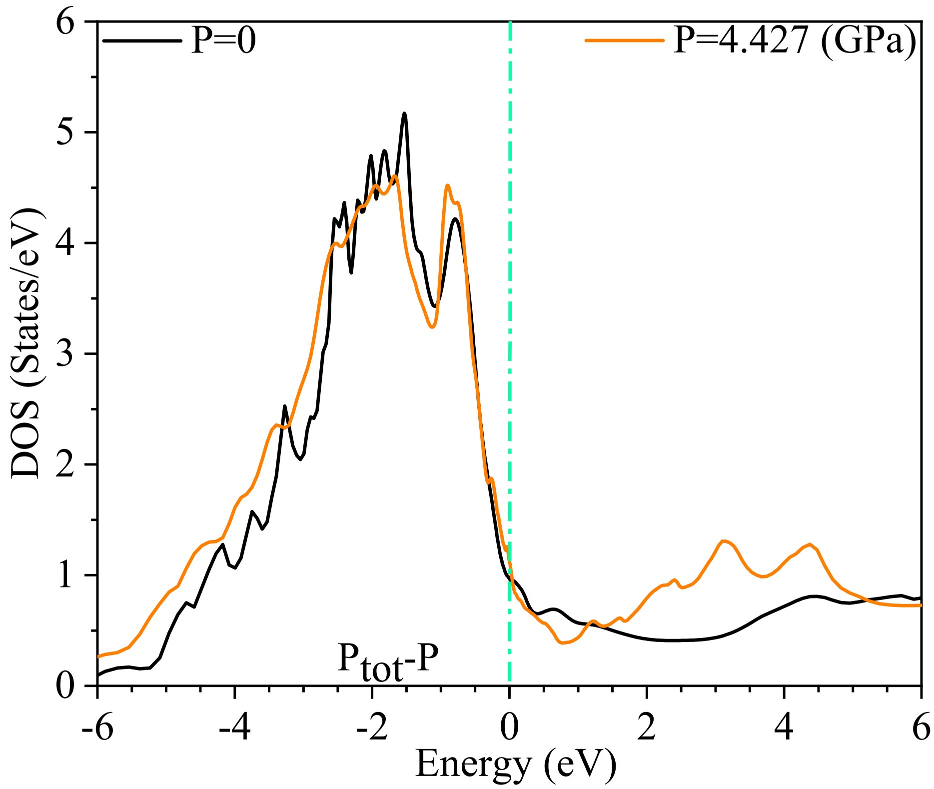

FIG. SM8. The pressure-dependent projected DOS of the ligand p orbitals for UP_2 in the tetragonal $I4/mmm$ structure. The vertical dashed–dotted lines denote the Fermi level. All results are obtained from fully charge-self-consistent DFT+DMFT calculations using PBE–GGA and including SOC.

cupied region displays a moderate enhancement of spectral weight centered around −2 eV, where the d states overlap with the upper portion of the ligand p valence band. This overlap reflects the hybridized nature of the U–P bonding network in the tetragonal $I4/mmm$ structure. The overall amplitude of the d DOS remains significantly smaller than that of the uranium $5f$ states discussed previously, emphasizing that the d orbitals do not dominate the low-energy quasiparticle formation. Near the Fermi level, the d contribution is characterized by a shallow minimum, confirming that the Fermi-surface states are primarily $5f$-derived with only a minor admixture of d character.

Applying hydrostatic pressure introduces systematic yet moderate modifications to this spectral profile. The most evident effect is an overall amplification of the d-derived spectral weight across both the occupied and unoccupied energy ranges. In the valence region between roughly −4 and −1 eV, the compressed lattice leads to a noticeable increase in DOS amplitude together with a mild smoothing of the spectral features. This behavior reflects enhanced orbital overlap as the U–P and U–U interatomic distances decrease. Because the radial extent of the $6d$ orbitals is larger than that of the $5f$ states, they respond particularly sensitively to structural compression, broadening and redistributing their spectral weight across the hybridized valence band.

The unoccupied region above the Fermi level shows an even more pronounced response. Between approximately 1 and 5 eV, the pressure-enhanced spectrum develops a higher overall intensity and a slightly more structured profile. This increase in unoccupied d weight signals a strengthening of the itinerant conduction channels that couple to the correlated $5f$ electrons. In a DMFT framework, such changes effectively modify the electronic bath that hybridizes with the $5f$ impurity orbitals, thereby influencing the screening environment that governs many-body renormalization processes.

Despite these global changes, the spectral behavior in the immediate vicinity of the Fermi level remains relatively stable. The d-projected DOS continues to exhibit a shallow minimum at E_F, indicating that the uranium $6d$ orbitals do not themselves generate the coherent quasiparticle peak. Nevertheless, a slight upward shift of the d spectral intensity near E_F can be discerned under compression. This subtle enhancement suggests a modest increase in d participation in the hybridized conduction network, reinforcing the overall

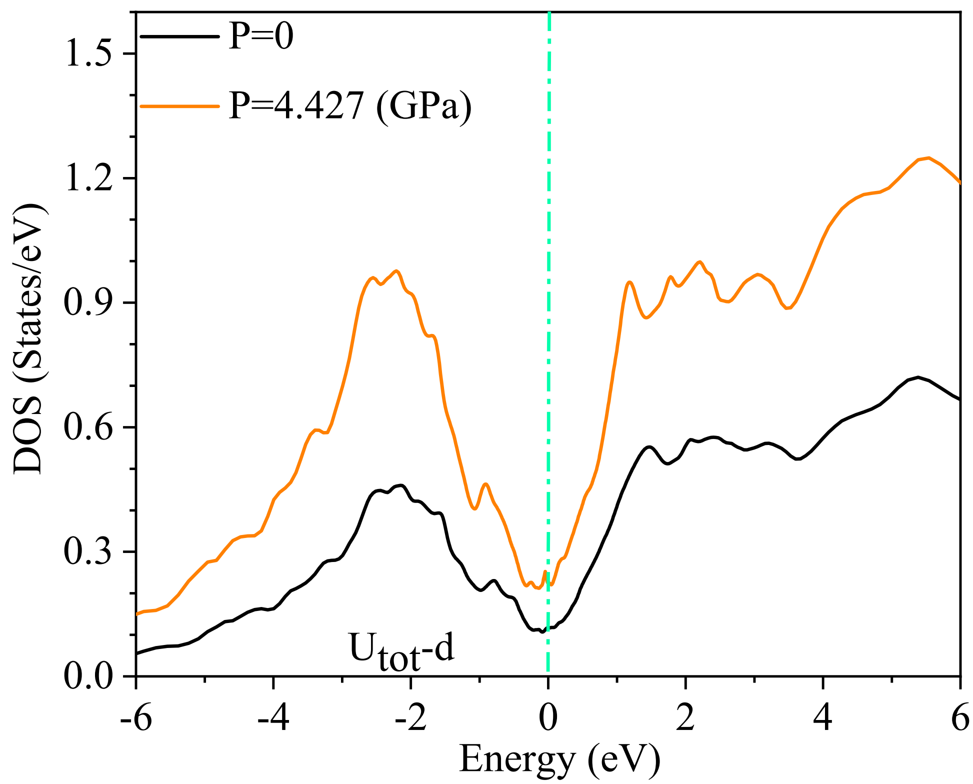

FIG. SM9. The projected DOS of the U d states at ambient pressure (black) and under hydrostatic compression $P = 4.427$ GPa (orange) for UP_2 in the tetragonal $I4/mmm$ structure. The vertical dashed–dotted lines denote the Fermi level. All results are obtained from fully charge-self-consistent DFT+DMFT calculations using PBE–GGA and including SOC.

electronic connectivity among the p, d, and $5f$ sectors.

When considered alongside the previously discussed ligand p DOS (Fig. SM8) and the total spectral evolution (Fig. SM7), the d-orbital response fits naturally into a broader picture of pressure-induced electronic restructuring in UP_2. Rather than dramatically altering any single orbital channel, hydrostatic compression gradually strengthens the hybridization pathways linking the ligand, uranium d, and uranium $5f$ states. The extended $6d$ orbitals, by virtue of their spatial reach and energetic proximity to the conduction bands, act as a bridge that facilitates this enhanced coupling. As the hybridization network becomes more effective, the correlated $5f$ electrons experience stronger screening and develop a more coherent quasiparticle character at low energy.

This cooperative evolution highlights a key characteristic of actinide systems: the emergent electronic behavior arises from the interplay of multiple orbital sectors rather than from isolated changes within the correlated $5f$ shell alone. The ligand p states provide the primary conduction bath, the uranium d orbitals mediate and broaden the hybridization landscape, and the uranium $5f$ electrons supply the strongly correlated degrees of freedom that shape the low-energy physics.

With this broader hybridization framework established, the next step is to examine the uranium $5f$ manifold itself in greater detail. By resolving the $5f$ spectral function into its spin–orbit–split $j = 5/2$ and $j = 7/2$ components under pressure, we can directly identify how the internal structure of the correlated $5f$ states evolves and determine whether the enhanced quasiparticle coherence arises from redistribution of spectral weight, shifts of multiplet features, or deeper many-body renormalization effects within the spin–orbit–coupled $5f$ shell.

Figure SM10 [Fig. B1(b_2) of the main paper] presents the spin–orbit–resolved uranium $5f$ spectral functions at ambient pressure and under compression, offering a direct view of how hydrostatic pressure modifies the correlated $5f$ electronic structure in UP_2. Since the uranium $5f$ states dominate the low-energy electronic structure of actinide systems, monitoring the evolution of the $j = 5/2$ and $j = 7/2$ components provides important insight into how compression alters quasiparticle coherence and redistributes spectral weight within the SOC-split $5f$ manifold.

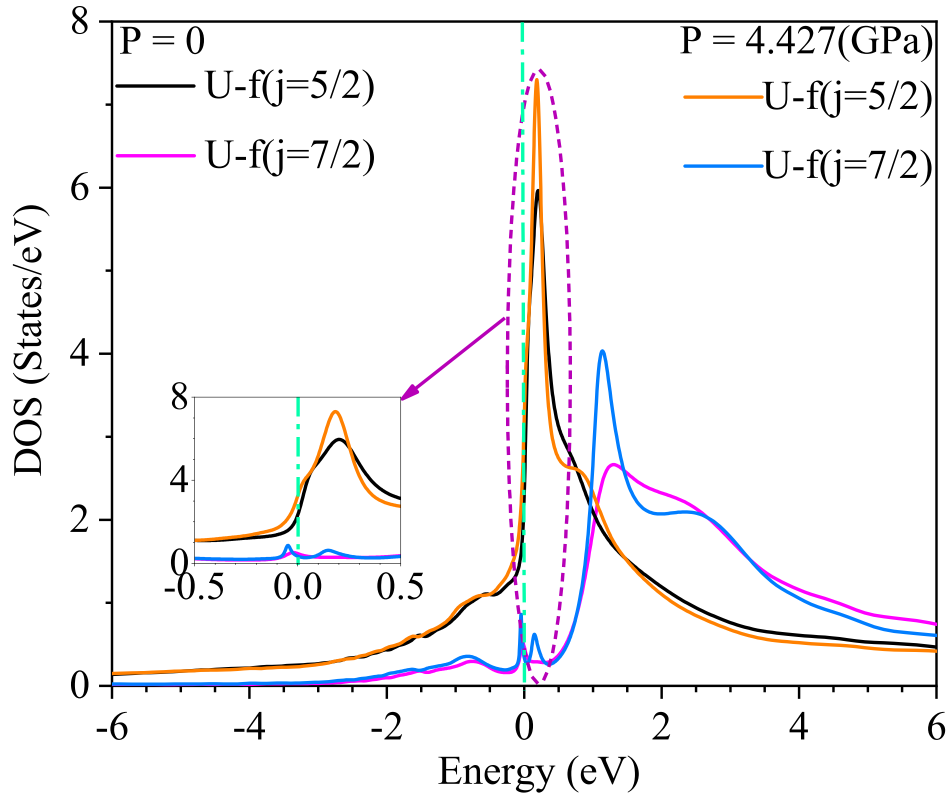

FIG. SM10. Pressure-induced redistribution of spectral weight within the U $5f$ manifold of UP_2 in the tetragonal $I4/mmm$ structure. The spin–orbit–resolved components $j = 5/2$ and $j = 7/2$ are shown for ambient pressure ($P = 0$) and under compression ($P = 4.427$ GPa). The inset magnifies the low-energy region around the Fermi level to highlight changes in the quasiparticle resonance. The vertical dashed–dotted line indicates the Fermi level. All results are obtained from fully charge-self-consistent DFT+DMFT calculations using PBE–GGA with spin–orbit coupling included.

At ambient pressure ($P = 0$), the $j = 5/2$ component (black) dominates the spectral weight in the vicinity of the Fermi level. A pronounced quasiparticle peak emerges slightly below E_F, indicating that the low-energy electronic states are primarily derived from the $j = 5/2$ manifold. This sharp resonance reflects the correlated metallic nature of the system, where the $5f$ electrons retain substantial itinerancy while still experiencing strong many-body renormalization. In contrast, the $j = 7/2$ states (magenta) appear mainly at higher energies above the Fermi level and display a broader distribution of spectral weight. This separation reflects the strong spin–orbit splitting characteristic of uranium $5f$ shells, which energetically stabilizes the $j = 5/2$ states relative to the $j = 7/2$ manifold.

Applying hydrostatic pressure ($P = 4.427$ GPa) leads to a clear restructuring of the $5f$ spectral distribution. The $j = 5/2$ quasiparticle peak (orange) becomes more intense and slightly sharper near the Fermi level, indicating enhanced quasiparticle coherence. This behavior signals an increase in effective hybridization between the uranium $5f$ states and the surrounding conduction electrons, which strengthens the many-body screening processes captured within DMFT. The enhanced low-energy coherence is consistent with the pressure-induced strengthening of the uranium–ligand hybridization network discussed earlier for the ligand p and uranium d states.

The $j = 7/2$ component (blue) also exhibits noticeable modifications under compression. Its spectral weight becomes more pronounced in the unoccupied region around 1–1.5 eV and shows a modest shift toward lower energies. Although these states remain largely above the Fermi level and therefore do not directly participate in the quasiparticle peak, their increased intensity indicates stronger participation in hybridization processes. This redistribution effectively broadens the energy window over which the $5f$ shell interacts with the conduction bath.

The inset highlights the immediate vicinity of the Fermi level, where the most important correlation effects occur. The comparison clearly shows that pressure amplifies the $j = 5/2$ quasiparticle resonance while leaving only a very small $j = 7/2$ contribution near E_F. This reinforces the picture that the low-energy electronic properties of UP_2 remain dominated by the $j = 5/2$ manifold, while the $j = 7/2$ states primarily influence higher-energy excitations.

Overall, the figure illustrates that hydrostatic compression does not qualitatively alter the SOC-split structure of the uranium $5f$ shell, but it significantly redistributes spectral weight and enhances quasiparticle coherence within the dominant $j = 5/2$ channel. The combined effect is a pressure-driven strengthening of the hybridization between the $5f$ electrons and the conduction environment, pushing the system toward a more coherent itinerant regime.

Having established how pressure reshapes the internal structure of the $5f$ spectral weight, we next analyze the impurity hybridization function $\Delta(\omega)$, which directly quantifies the dynamical coupling between the correlated $5f$ shell and the surrounding conduction bath. This quantity provides a microscopic explanation for the enhanced quasiparticle coherence observed in the spectral functions.

SM II. Spin–Orbit–Selective Hybridization and Bath Coupling of the Uranium $5f$ Shell

Figure SM11 [Fig. B1(b$_3$) of the main paper] displays the impurity hybridization spectrum $-\Im[\Delta(\omega)]$ for the $j = 5/2$ component of the uranium $5f$ shell, which provides a direct measure of the dynamical coupling between the correlated $5f$ electrons and the itinerant electronic bath of the lattice. Within the DMFT impurity framework defined by Eqs. (2) and (4), as expressed in the main paper, the hybridization function $\Delta(\omega)$ encodes how the correlated impurity orbital exchanges electrons with the surrounding conduction states. Its imaginary part therefore represents the energy-resolved hybridization spectral density governing charge fluctuations between the localized $5f$ orbitals and the itinerant bands, which in the present system arise predominantly from uranium d and phosphorus p states. The magnitude and frequency dependence of $-\Im[\Delta(\omega)]$ thus provide a microscopic view of how the correlated uranium $5f$ shell is embedded within the surrounding electronic environment.

At ambient pressure ($P = 0$), the hybridization spectrum exhibits a highly structured profile extending across the entire energy window from approximately -6 to $+6$ eV. In the deep valence region the hybridization amplitude is relatively small but steadily increases as the energy approaches the main valence band complex. Between roughly -4 and -1 eV the spectrum develops a sequence of pronounced peaks and shoulders, indicating strong mixing between uranium $5f$ states and the ligand-dominated valence bands. This region corresponds closely to the energy range where the projected density of states shows significant phosphorus p character, confirming that the hybridization features originate primarily from $5f$–p bonding interactions. The gradual rise of the hybridization strength toward the Fermi level reflects the increasing overlap between the uranium orbitals and the itinerant states forming the top of the valence band.

Near the Fermi level the hybridization function remains clearly finite and reaches one of its largest values. This strong low-energy coupling is a central feature of the electronic structure because it allows the $j = 5/2$ states to communicate efficiently with the conduction bath. In the DMFT description, such finite hybridization at $\omega \approx 0$ provides the dynamical channel required for screening of the local Coulomb interaction and for the formation of coherent quasiparticle excitations. The sizable value of $-\Im[\Delta(\omega)]$ in this region therefore explains why the $j = 5/2$ manifold dominates the low-energy spectral weight and forms the quasiparticle peak observed in the density of states around E_F. The structured dip appearing very close to $\omega = 0$ reflects the detailed band structure of the itinerant states that form the effective bath, rather than a suppression of coupling, and arises from the specific distribution of conduction bands intersecting the Fermi level.

In the unoccupied region above the Fermi level the hybridization spectrum again increases and develops broad maxima extending up to about 6 eV. These structures originate primarily from coupling between the $5f$ orbitals and higher-energy conduction states containing significant uranium d character, together with antibonding combinations involving ligand orbitals. The persistence of substantial hybridization over such a wide energy range highlights the extended spatial character of the uranium $5f$ orbitals, which enables them to overlap efficiently with both valence and conduction states of the surrounding lattice. Consequently, the $j = 5/2$ manifold interacts with a broad spectrum of bath states, producing the rich frequency dependence observed in the hybridization function.

Applying hydrostatic pressure ($P = 4.427$ GPa) produces a systematic enhancement of the hybridization amplitude throughout nearly the entire spectrum. The orange curve consistently lies above the ambient-pressure result, indicating that the dynamical coupling between the uranium $5f$ orbitals and the conduction bath becomes stronger under lattice compression. The enhancement is most pronounced in the occupied region below the Fermi level, particularly within the multi-peak structure between approximately -3 and -1 eV, where the hybridization features become sharper and larger in magnitude. This behavior directly reflects the increase of orbital overlap between uranium and phosphorus atoms as the lattice parameters contract, strengthening the $5f$–p hopping processes that dominate the bonding states of the valence band. A comparable amplification is also observed in the unoccupied energy range above E_F, indicating that the coupling between $5f$ orbitals and higher-energy conduction states is likewise reinforced by compression.

Although the overall spectral shape of the hybridization function remains essentially unchanged, the global increase in magnitude signifies a stronger embedding of the correlated $5f$ electrons into the itinerant electronic environment. Even the modest enhancement visible close to the Fermi level is physically significant because the low-energy hybridization directly controls the efficiency of dynamical screening in DMFT. Increased hybridization therefore promotes stronger quasiparticle coherence and reduces the degree of effective localization of the $5f$ electrons. This trend is fully consistent with the pressure evolution observed in the density of states,

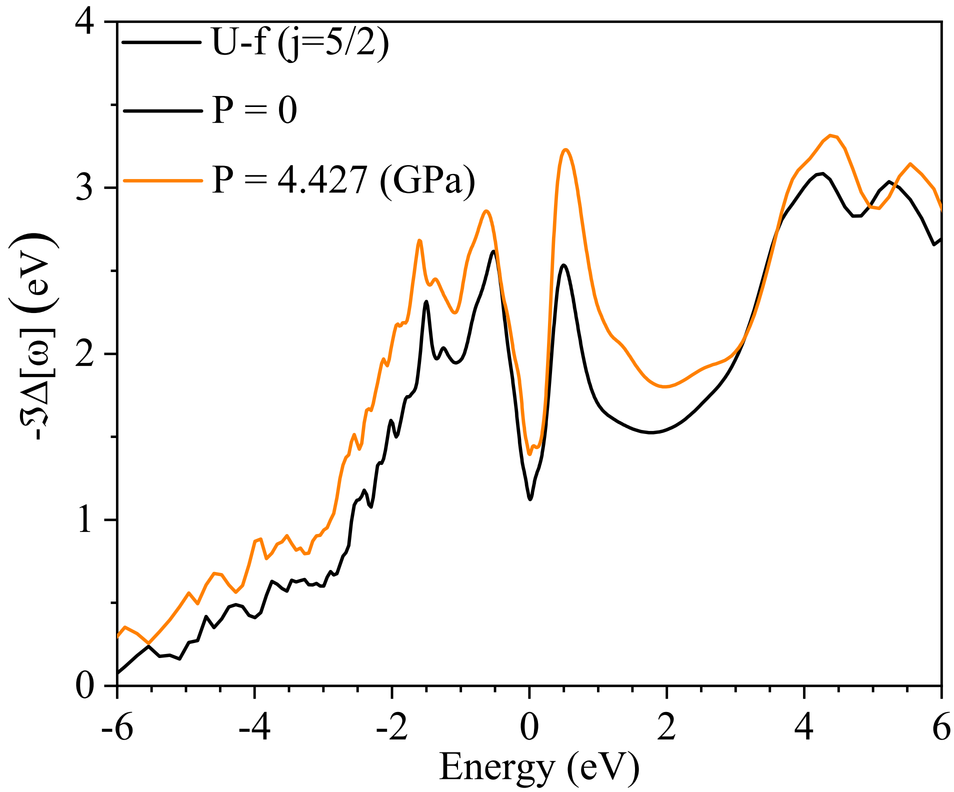

FIG. SM11. Impurity hybridization spectrum $-\Im[\Delta(\omega)]$ for the uranium $5f$ $j = 5/2$ manifold in UP_2, evaluated within the DMFT impurity mapping defined by the Dyson equation [Eq. (2) of the main paper] and the hybridization embedding relation [Eq. (4) of the main paper]. The black curve shows the ambient-pressure result ($P = 0$), while the orange curve corresponds to hydrostatic compression at $P = 4.427$ GPa. The spectrum exhibits rich structure extending across the valence and conduction energy ranges, reflecting the frequency-dependent coupling between the correlated U $5f$ orbitals and the itinerant bath composed primarily of U d and P p states. Compression systematically enhances the hybridization amplitude over a broad energy window—most notably within the occupied region below the Fermi level—indicating increased U–P orbital overlap and stronger embedding of the $5f$ electrons into the conduction environment. All data are obtained from fully charge-self-consistent DFT+DMFT calculations using PBE–GGA and including spin–orbit coupling.

where the quasiparticle peak associated with the $j = 5/2$ manifold becomes sharper and slightly more intense as the lattice is compressed.

In conclusion, the results shown in Fig. SM11 demonstrate that hydrostatic pressure primarily acts to strengthen the coupling between uranium $5f$ orbitals and the surrounding conduction states without qualitatively altering the structure of the hybridization spectrum. The $j = 5/2$ manifold therefore remains the dominant low-energy channel through which the correlated uranium electrons interact with the itinerant bath, and its enhanced hybridization under pressure drives the gradual evolution toward a more itinerant electronic regime in UP_2.

While the $j = 5/2$ manifold dominates the low-energy quasiparticle dynamics, the $j = 7/2$ component represents the "excited" sector of the spin–orbit-split $5f$ shell, typically residing at higher energies. The following analysis of the $j = 7/2$ hybridization function $-\Im[\Delta_{j=7/2}(\omega)]$ reveals a distinct spectral profile characterized by a shift in weight toward unoccupied states and a different sensitivity to lattice compression. By comparing the two SOC-resolved channels, we can identify how pressure differentially affects the bonding and antibonding environments of the uranium ion, ultimately dictating the orbital-selective nature of the itinerancy–localization crossover in UP_2.

The hybridization spectrum for the $j = 7/2$ manifold shown in Fig. SM12 [Fig. B1(b_4) of the main paper] provides further insight into how the excited spin–orbit sector of the uranium $5f$ shell interacts dynamically with the surrounding itinerant electronic environment in UP_2. Within the DMFT impurity formulation, the hybridization function $\Delta(\omega)$ characterizes the frequency-dependent coupling between the correlated impurity orbitals and the conduction bath generated by the lattice. Its imaginary part, $-\Im[\Delta(\omega)]$, therefore rep-

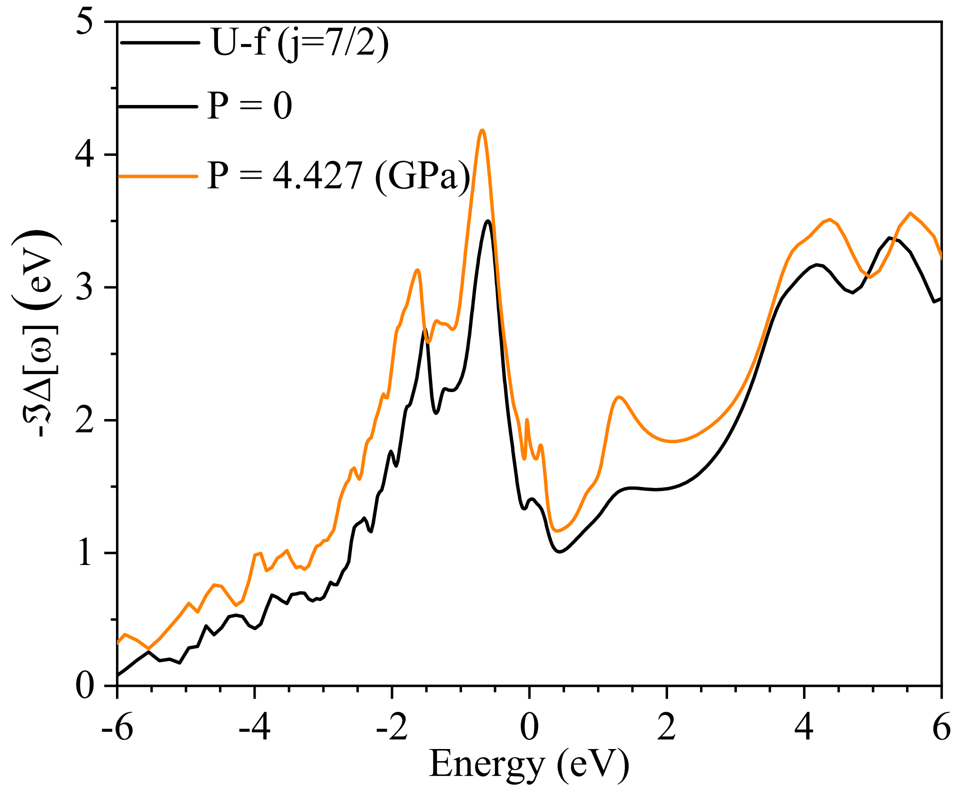

FIG. SM12. Energy dependence of the impurity hybridization function $-\Im[\Delta(\omega)]$ for the uranium $5f$ $j = 7/2$ manifold in UP_2 crystallizing in the tetragonal $I4/mmm$ structure. The hybridization function is obtained from the DMFT impurity mapping defined by the impurity Dyson equation [Eq. (2) of the main paper] and its embedding relation [Eq. (4) of the main paper]. Black and orange curves correspond to ambient pressure ($P = 0$) and hydrostatic compression at $P = 4.427$ GPa, respectively. The spectrum exhibits pronounced energy-dependent structures extending from the valence region below the Fermi level to several electronvolts above it, reflecting the dynamical coupling between uranium $5f$ states and the surrounding conduction bath dominated by U d and P p orbitals. Under compression the overall magnitude of $-\Im[\Delta(\omega)]$ increases across a broad energy window, indicating enhanced hybridization between the correlated $5f$ shell and the itinerant environment due to reduced U–P bond distances. All results are obtained from fully charge-self-consistent DFT+DMFT calculations using PBE–GGA and including spin–orbit coupling.

resents the hybridization spectral density that governs the probability for electrons to fluctuate between the localized $5f$ orbitals and the itinerant states. The detailed structure of this function reflects the distribution of bath states available for hybridization and thus provides direct microscopic information about how the correlated uranium orbitals are embedded within the broader electronic structure composed primarily of U d and ligand P p bands.

The hybridization spectrum associated with the $j = 7/2$ manifold extends across a wide energy window from approximately −6 eV in the deep valence region to about 6 eV in the unoccupied conduction states. The spectrum exhibits a pronounced and highly structured profile with multiple peaks and shoulders distributed across both occupied and unoccupied energies. In the valence region the hybridization amplitude increases steadily from the deep binding energies toward the upper valence band, reaching a strong maximum in the interval between roughly −2 and −0.5 eV. This behavior mirrors the increasing density of ligand-dominated valence states in this energy range and indicates significant hybridization between uranium $5f$ orbitals and the phosphorus p bands that participate in bonding. The pronounced peak structure in this region therefore reflects the strong $5f$–p mixing responsible for the formation of bonding states in the compound.

Approaching the Fermi level the hybridization function displays a sharp suppression followed by a narrow dip near $\omega \approx 0$, which reflects the detailed structure of the conduction bath around the Fermi energy. Although the hybridization remains finite in this region, its magnitude is noticeably smaller than in the nearby valence peaks and also somewhat weaker than the corresponding value for the $j = 5/2$ manifold. This difference originates from the spin–orbit splitting of the uranium $5f$ shell. Because the $j = 7/2$ multiplet lies energetically above the $j = 5/2$ states, its overlap with the low-energy conduction states that form the quasiparticle band is reduced. As a result, the $j = 7/2$ orbitals participate less strongly in the formation of coherent low-energy quasiparticle excitations, while the $j = 5/2$ states remain the dominant channel governing the electronic properties in the immediate vicinity of the Fermi level.

In the unoccupied region above E_F, the hybridization spectrum again increases substantially and develops broad maxima between approximately 3 and 5 eV. These features arise primarily from coupling between the uranium $5f$ orbitals and higher-energy conduction states containing strong U d character, together with antibonding combinations involving ligand orbitals. The presence of significant hybridization in this energy range highlights the extended spatial character of uranium $5f$ orbitals, which enables them to interact with a wide variety of conduction states across a large energy interval. Consequently, the $j = 7/2$ manifold exhibits a hybridization profile that is broadly distributed in energy, reflecting its interaction with both valence and high-energy conduction bands.

Applying hydrostatic pressure ($P = 4.427$ GPa) produces a clear and systematic enhancement of the hybridization amplitude across almost the entire energy range. The orange curve consistently lies above the ambient-pressure spectrum, demonstrating that the dynamical coupling between the uranium $5f$ shell and the conduction bath becomes stronger when the lattice is compressed. This enhancement is particularly visible in the prominent valence peaks around −2 to −1 eV as well as in the conduction-band structures above 3 eV, where the hybridization maxima increase noticeably in magnitude. Microscopically, this behavior reflects the reduction of U–P bond distances under compression, which increases the overlap between uranium $5f$ orbitals and the surrounding ligand orbitals. The strengthened orbital overlap enhances the effective hopping processes that mediate hybridization between the impurity and the bath, thereby embedding the correlated $5f$ states more strongly within the itinerant electronic environment.

Despite the overall increase in hybridization strength, the qualitative structure of the spectrum remains largely preserved under pressure. The positions of the dominant peaks and the overall distribution of spectral weight change only moderately, indicating that compression primarily amplifies the existing hybridization channels rather than generating new ones. Importantly, the relative hierarchy between the two spin–orbit manifolds remains essentially unchanged. Even though the $j = 7/2$ hybridization increases in magnitude, its coupling near the Fermi level remains weaker than that of the $j = 5/2$ states. This persistent difference underscores the spin–orbit–controlled orbital selectivity of the uranium $5f$ shell, where the $j = 5/2$ manifold continues to dominate the low-energy quasiparticle dynamics while the $j = 7/2$ sector contributes mainly to higher-energy excitations.

In essence, with the hybridization spectrum of the $j = 5/2$ manifold discussed previously, these results reveal a coherent picture of how the uranium $5f$ shell is dynamically embedded within the multiorbital conduction environment of UP_2. The strongly structured hybridization functions reflect the complex interplay between uranium $5f$, uranium d, and ligand p states that collectively form the electronic bath. Hydrostatic pressure enhances the coupling between these subsystems by strengthening orbital overlap, thereby promoting a more itinerant electronic regime while preserving the intrinsic spin–orbit hierarchy within the $5f$ shell. Once the frequency-dependent embedding of the correlated orbitals has been characterized, the next step is to examine the resulting many-body self-energy, which directly determines quasiparticle renormalization, electronic coherence, and the strength of correlation effects within the DMFT description of UP_2.

SMVIII. MATSUBARA SELF-ENERGY, QUASIPARTICLE RENORMALIZATION, AND FERMI-LIQUID COHERENCE

Figure SM13 [Fig. B1(c_1) of the main paper] displays the imaginary part of the Matsubara self-energy, $\Im[\Sigma_{5/2}(i\omega_n)]$, for the uranium $5f$ $j = 5/2$ manifold of UP_2 at ambient pressure ($P = 0$), obtained from fully charge-self-consistent DFT+DMFT calculations including spin–orbit coupling. The Matsubara self-energy provides a direct measure of the dynamical many-body effects acting on the correlated $5f$ electrons and therefore serves as a key quantity for characterizing the strength of electronic correlations and the coherence of low-energy quasiparticles.

The main panel of Fig. SM13 shows the Matsubara-frequency dependence of the matrix-valued impurity self-energy $\Im[\Sigma_{\mathrm{imp},mm'}(i\omega_n)]$ within the $j = \frac{5}{2}$ manifold. In the main manuscript the Green's functions and related quantities are written as functions of the real frequency ω. In the present discussion, however, we work on the imaginary-frequency (Matsubara) axis used in the CT-QMC impurity solver, where $\omega \to i\omega_n$ with fermionic Matsubara frequencies $\omega_n = (2n+1)\pi T$ at temperature T (with $k_B = 1$). At low frequencies the imaginary part reaches its largest magnitude, reflecting strong quasiparticle renormalization near the Fermi level. With increasing ω_n all components decrease smoothly and follow the characteristic $1/\omega_n$ decay expected for the dynamical part of the self-energy. Importantly, the full self-energy does not vanish at large frequencies; instead it approaches a finite static matrix Σ_∞ while only its imaginary part tends to zero. In multiorbital DMFT, this static limit Σ_∞ represents the high-frequency (instantaneous) interaction contribution generated by the local Coulomb tensor $U_{mm'm''m'''}$ and depends on the orbital occupancies, Hund's coupling, and the chosen spin–orbit–coupled basis. Consequently, Σ_∞ is generally finite and need not be diagonal unless enforced by symmetry; it vanishes only in the non-interacting limit ($U, J = 0$) or in special mean-subtracted interaction schemes not used in modern DFT+DMFT.

The origin of this behavior follows directly from the high-frequency structure of the local impurity Green's function introduced in Sec. II A of the main manuscript. The interacting Green's function $\mathcal{G}(i\omega_n)$ admits the spectral repre-

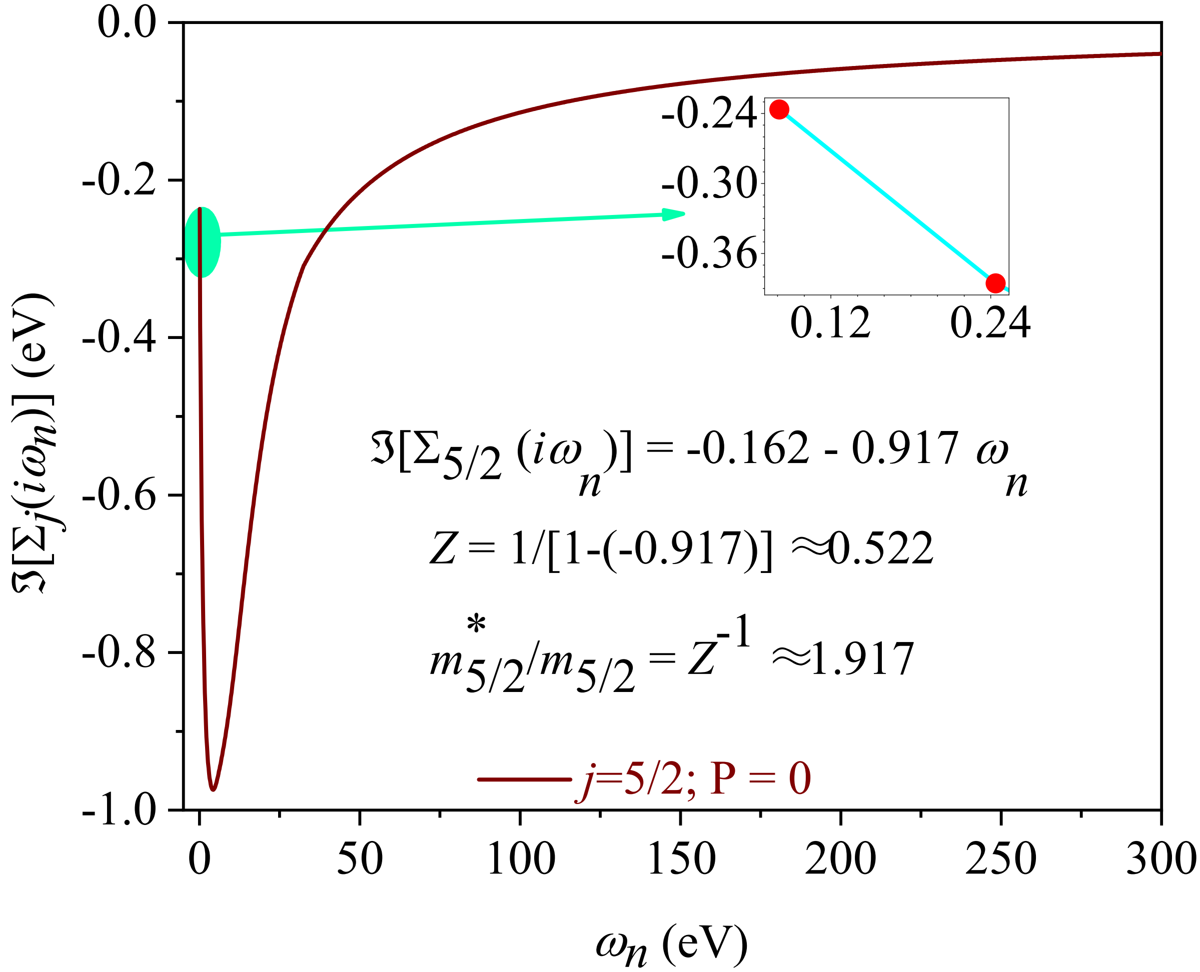

FIG. SM13. The imaginary part of the uranium $5f$ Matsubara self-energy ($\Im[\Sigma_{5/2}(i\omega_n)]$) at ambient pressure ($P = 0$). The curve displays the frequency dependence of the self-energy for the $j = 5/2$ manifold, obtained from fully charge-self-consistent DFT+DMFT calculations using PBE–GGA and including SOC. The inset magnifies the low-frequency region near $\omega_n \to 0$, highlighting the linear behavior characteristic of a Fermi liquid. The red circles indicate the linear fit used to extract the quasiparticle renormalization factor Z via its relation to the slope at $\omega_n \to 0$, as defined in Eq. (A3) of the main paper and consistent with the general definition in Eq. (13) of the main paper. The extracted values are $\Im[\Sigma_{5/2}(i\omega_n)] = -0.162 - 0.917\omega_n$, yielding $Z \approx 0.522$ and a mass enhancement $m^*_{5/2}/m_0 = Z^{-1} \approx 1.917$.

sentation

$$\mathcal{G}(i\omega_n) = \int_{-\infty}^{+\infty} \frac{\mathrm{A}(\omega')}{i\omega_n - \omega'}\, d\omega', \tag{SM9}$$

where $\mathrm{A}(\omega)$ is the local spectral function projected onto the correlated $5f$ subspace. Expanding the resolvent for large $|i\omega_n|$,

$$\frac{1}{i\omega_n - \omega'} = \frac{1}{i\omega_n}\left(1 + \frac{\omega'}{i\omega_n} + \frac{\omega'^2}{(i\omega_n)^2} + \cdots\right), \tag{SM10}$$

yields the moment expansion

$$\mathcal{G}(i\omega_n) = \frac{\mathbf{M}_0}{i\omega_n} + \frac{\mathbf{M}_1}{(i\omega_n)^2} + \frac{\mathbf{M}_2}{(i\omega_n)^3} + \cdots, \tag{SM11}$$

where $\mathbf{M}_k = \int d\omega\, \omega^k \mathrm{A}(\omega)$. Using the spectral sum rule $\mathbf{M}_0 =$ $\mathbf{I}$ gives

$$\mathcal{G}(i\omega_n) = \frac{\mathbf{I}}{i\omega_n} + \frac{\mathbf{M}_1}{(i\omega_n)^2} + \frac{\mathbf{M}_2}{(i\omega_n)^3} + \cdots. \tag{SM12}$$

Inserting Eq. (SM12) into the multiorbital impurity Dyson equation introduced in the main text [Eq. (2)], requires the corresponding high-frequency behavior of the hybridization function $\Delta(\omega)$ defined in Eq. (4) of the main paper. From that expression one can expand the resolvent of the bath propagator. Expanding $(i\omega_n - \varepsilon_k)^{-1} = \frac{1}{i\omega_n} + \frac{\varepsilon_k}{(i\omega_n)^2} + \cdots$ yields

$$\Delta(i\omega_n) = \frac{\Delta_1}{i\omega_n} + \frac{\Delta_2}{(i\omega_n)^2} + \cdots. \tag{SM13}$$

Using Eq. (SM12), the inverse Green's function can be expanded as

$$\mathcal{G}^{-1}(i\omega_n) = i\omega_n \mathbf{I} - \mathbf{M}_1 + \frac{\mathbf{M}_1^2 - \mathbf{M}_2}{i\omega_n} + O\left(\frac{1}{(i\omega_n)^2}\right). \quad \text{(SM14)}$$

Substituting this result together with the hybridization expansion into Eq. (2), as expressed in the main paper, and solving order by order in $1/i\omega_n$ gives the large-frequency expansion of the impurity self-energy

$$\Sigma_{\text{imp}}(i\omega_n) = \Sigma_\infty + \frac{\Sigma_1}{i\omega_n} + \frac{\Sigma_2}{(i\omega_n)^2} + \cdots, \quad \text{(SM15)}$$

where

$$\Sigma_\infty = \mu \mathbf{I} - \mathbf{E}_{\text{imp}} + \mathbf{M}_1. \quad \text{(SM16)}$$

Since $1/(i\omega_n) = -i/\omega_n$, the leading dynamical correction is purely imaginary and therefore

$$\Im[\Sigma_{\text{imp},mm'}(i\omega_n)] \propto \frac{1}{\omega_n} \qquad (\omega_n \to \infty). \quad \text{(SM17)}$$

Consequently, the imaginary part of the self-energy decays as $1/\omega_n$, while the full self-energy approaches the finite constant matrix Σ_∞, consistent with the universal high-frequency asymptotics of the multiorbital DMFT self-energy and with the numerical behavior shown in Fig. SM13.

The most physically relevant information, however, is contained in the low-frequency regime highlighted in the inset of Fig. SM13. In this region the self-energy exhibits a well-defined linear dependence on the Matsubara frequency. Such linear behavior is the hallmark of a Fermi-liquid state, where the electronic excitations can be described in terms of long-lived quasiparticles whose properties are renormalized by electronic interactions. In this limit the self-energy can be expanded around $\omega_n \to 0$, and the slope of $\Im[\Sigma(i\omega_n)]$ directly determines the quasiparticle renormalization factor through the relation given in Eq. (A3) of the main paper.

To quantify the renormalization strength, the lowest Matsubara points—marked by the red circles in the inset—are fitted with a linear function,

$$\Im[\Sigma_{5/2}(i\omega_n)] = -0.162 - 0.917\,\omega_n. \quad \text{(SM18)}$$

The intercept of the fit corresponds to the residual imaginary self-energy at the first Matsubara frequency, while the slope reflects the dynamical renormalization of the quasiparticle dispersion. From this slope the quasiparticle weight is obtained as $Z \approx 0.522$, corresponding to a mass enhancement $m^*_{5/2}/m_0 = Z^{-1} \approx 1.917$. This result indicates that the low-energy quasiparticles associated with the $j = 5/2$ manifold possess an effective mass roughly twice the corresponding noninteracting band mass.

The magnitude of this renormalization places UP_2 in the regime of moderately correlated $5f$ systems. The quasiparticles remain well defined, as evidenced by the clear linear behavior of the self-energy at low frequency, yet their dynamics are substantially renormalized by electronic interactions. Microscopically, this behavior arises from the interplay between on-site Coulomb interactions within the uranium $5f$ shell and hybridization with surrounding itinerant states, primarily derived from uranium d and ligand phosphorus p orbitals. These hybridization processes allow the correlated $5f$ electrons to fluctuate dynamically between localized and itinerant configurations, producing the renormalized quasiparticle excitations captured by the DMFT self-energy.

An important aspect of the present result is that the $j = 5/2$ manifold exhibits the dominant correlation effects in the system. Because spin–orbit coupling splits the uranium $5f$ shell into $j = 5/2$ and $j = 7/2$ components, and because the $j = 5/2$ states lie closest to the Fermi level, they contribute most strongly to the low-energy electronic structure. The substantial mass enhancement extracted from the Matsubara self-energy therefore confirms that the correlated quasiparticle states near E_F originate primarily from the $j = 5/2$ sector.

These dynamical results are fully consistent with the orbital-resolved density-of-states and hybridization analyses discussed previously. In those quantities the $j = 5/2$ states were shown to dominate the spectral weight around the Fermi level and to exhibit strong hybridization with surrounding ligand states. The Matsubara self-energy provides a complementary and more direct measure of the many-body renormalization associated with these hybridization processes. Together, the results establish that at ambient pressure UP_2 forms a coherent correlated metallic state in which the $j = 5/2$ electrons behave as moderately heavy quasiparticles. This baseline characterization provides the reference point for evaluating how hydrostatic compression modifies the strength of dynamical correlations and the coherence of the quasiparticle excitations in the subsequent analysis.

After discussing the quasiparticle renormalization and Fermi-liquid coherence of the $j = 5/2$ manifold at ambient pressure, we now extend the analysis to the remaining spin–orbit component and to the pressure-dependent evolution of the self-energy. In particular, we first examine the Matsubara self-energy for the $j = 7/2$ manifold at $P = 0$, which provides insight into how the higher-energy spin–orbit sector contributes to the correlated electronic structure. We then analyze the corresponding self-energies for both $j = 5/2$ and $j = 7/2$ manifolds under hydrostatic compression at $P = 4.427$ GPa. This sequential comparison allows us to track how pressure modifies the quasiparticle renormalization, effective mass, and coherence properties of the uranium $5f$ electrons, and thereby clarifies the role of spin–orbit-resolved correlations in the pressure-induced evolution of the electronic structure of UP_2.

Figure SM14 [Fig. B1(c_2) of the main paper] presents the imaginary part of the Matsubara self-energy, $\Im[\Sigma_{7/2}(i\omega_n)]$, for the uranium $5f$ $j = 7/2$ manifold of UP_2 at ambient pressure ($P = 0$), obtained from fully charge-self-consistent DFT+DMFT calculations including spin–orbit coupling. In contrast to the previously discussed $j = 5/2$ sector—which dominates the low-energy electronic structure—the $j = 7/2$ manifold corresponds to the higher-energy spin–orbit component of the uranium $5f$ shell. Examining its self-energy therefore provides a complementary perspective on

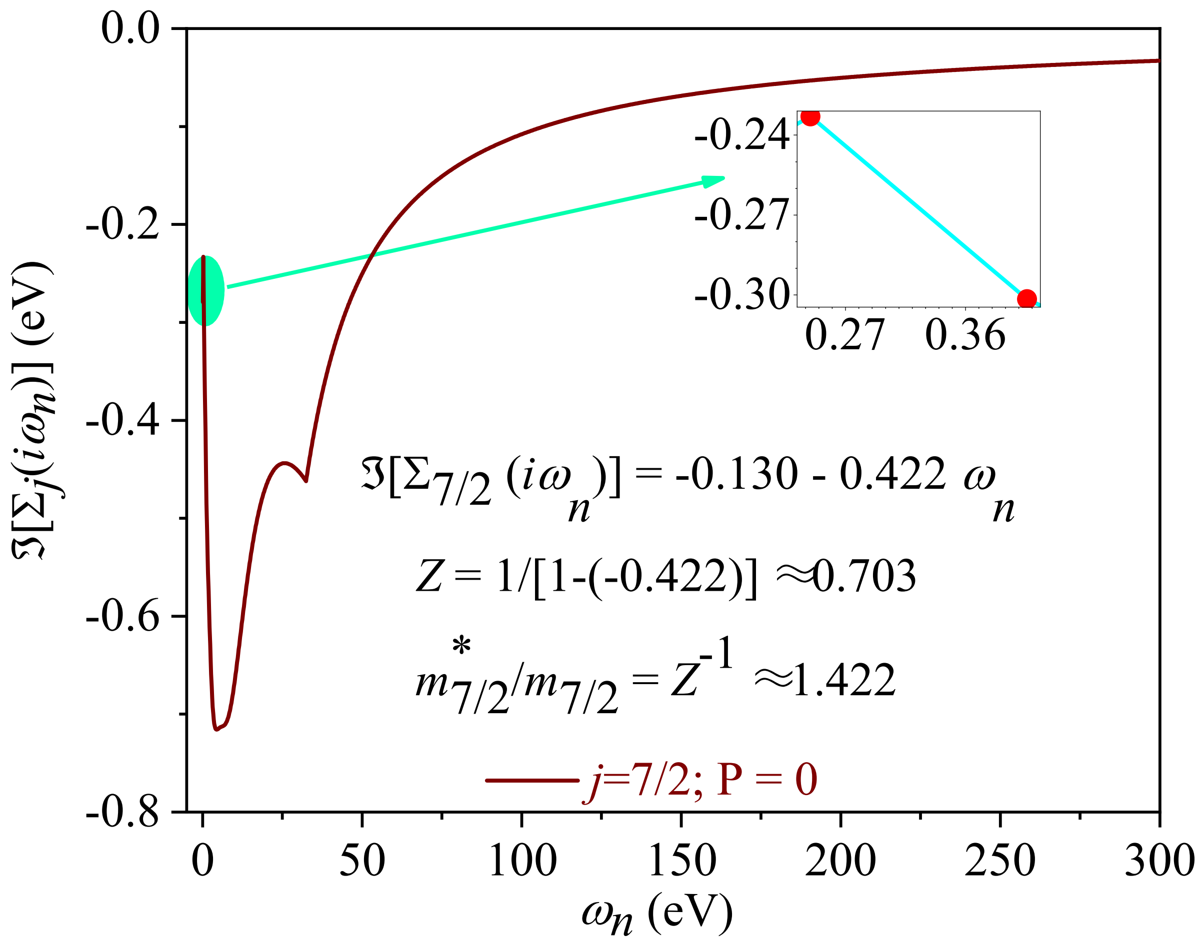

FIG. SM14. The imaginary part of the uranium $5f$ Matsubara self-energy, $\Im[\Sigma_{7/2}(i\omega_n)]$, for the $j = 7/2$ manifold of UP_2 at ambient pressure ($P = 0$). The main panel shows the full Matsubara-frequency dependence obtained from fully charge-self-consistent DFT+DMFT calculations using PBE–GGA and including SOC. The inset magnifies the low-frequency region near $\omega_n \to 0$, where the self-energy exhibits a linear behavior characteristic of a Fermi-liquid regime. The red circles indicate the linear slope in the Fermi-liquid regime used to extract the quasiparticle renormalization factor Z according to Eq. (A3), consistent with the formal definition in Eq. (13). All results are obtained from fully charge-self-consistent DFT+DMFT calculations using PBE–GGA and including SOC.

how electronic correlations are distributed between the two spin–orbit channels and clarifies the degree to which the higher-energy sector participates in the correlated quasiparticle dynamics.

The main panel displays the Matsubara-frequency dependence of $\Im[\Sigma_{7/2}(i\omega_n)]$. Similar to the $j = 5/2$ manifold, the self-energy exhibits its largest magnitude at the lowest Matsubara frequencies and gradually decreases toward zero as the frequency increases. This behavior reflects the generic structure of correlated metallic systems within DMFT, where low-energy quasiparticle excitations are strongly renormalized while higher-energy excitations progressively recover a more weakly interacting character. However, a clear distinction emerges when the overall magnitude of the self-energy is compared with that of the $j = 5/2$ manifold: throughout the entire frequency range, $\Im[\Sigma_{7/2}(i\omega_n)]$ remains noticeably smaller in magnitude. This difference indicates that the dynamical correlations acting on the $j = 7/2$ states are significantly weaker than those affecting the $j = 5/2$ sector.

The inset of Fig. SM14 highlights the low-frequency region, where the most relevant information about quasiparticle properties is contained. As in the $j = 5/2$ case, the self-energy displays a well-defined linear dependence on Matsubara frequency, confirming that the $j = 7/2$ states also obey Fermi-liquid behavior at low energies. The red circles mark the lowest Matsubara-frequency points used to perform the linear fit within this regime. Expanding the self-energy around $\omega_n \to 0$ yields

$$\Im[\Sigma_{7/2}(i\omega_n)] = -0.130 - 0.422\,\omega_n. \tag{SM19}$$

From the slope of this fit, the quasiparticle renormalization factor is obtained as $Z \approx 0.703$, corresponding to a mass enhancement $m^*_{7/2}/m_{7/2} = Z^{-1} \approx 1.422$.

A direct comparison with the $j = 5/2$ manifold reveals the spin–orbit-selective nature of the correlation effects in UP_2. While the $j = 5/2$ states exhibit a significantly larger slope in $\Im[\Sigma(i\omega_n)]$ and a stronger mass enhancement ($m^*/m \approx 1.917$), the $j = 7/2$ sector shows a noticeably weaker renormalization. The larger quasiparticle weight obtained for the $j = 7/2$ states therefore indicates that these electrons retain a more itinerant character and experience less pronounced many-body scattering.

This hierarchy can be understood from the relative energetic positions of the two spin–orbit manifolds. The $j = 5/2$ states lie closest to the Fermi level and therefore dominate the low-energy hybridization with surrounding conduction bands, leading to stronger dynamical renormalization. In contrast, the $j = 7/2$ states are located at somewhat higher energies and contribute less directly to the low-energy electronic structure. As a result, they experience weaker hybridization-driven correlation effects and display a smaller self-energy magnitude across the Matsubara-frequency range.

These observations are consistent with the orbital-resolved density-of-states and hybridization analyses presented earlier, where the $j = 5/2$ states were shown to provide the dominant spectral weight near the Fermi level while the $j = 7/2$ contributions appear mainly at higher energies. The Matsubara self-energy analysis thus reinforces the picture of spin–orbit-selective correlations in UP_2: the low-energy correlated quasiparticles originate primarily from the $j = 5/2$ manifold, whereas the $j = 7/2$ sector plays a more secondary role and remains comparatively weakly renormalized.

Considering this contrast between the two spin–orbit components at ambient pressure provides an essential reference point for analyzing the pressure dependence of the self-energy. Subsequently, we examine how hydrostatic compression modifies the quasiparticle renormalization and dynamical correlations of both the $j = 5/2$ and $j = 7/2$ manifolds, thereby revealing the pressure-driven evolution of spin–orbit-resolved correlation effects in UP_2.

Figure SM15 [Fig. B1(c$_3$) of the main paper] shows the imaginary part of the Matsubara self-energy, $\Im[\Sigma_{5/2}(i\omega_n)]$, for the uranium $5f$ $j = 5/2$ manifold of UP_2 under hydrostatic compression at $P = 4.427$ GPa. This analysis extends the ambient-pressure results and allows a direct assessment of how external pressure modifies the dynamical many-body renormalization of the dominant spin–orbit channel. Since the $j = 5/2$ states form the principal low-energy sector of the uranium $5f$ shell, their self-energy behavior provides the most direct measure of the pressure evolution of quasiparticle coherence in the system.

The main panel presents the full Matsubara-frequency dependence of $\Im[\Sigma_{5/2}(i\omega_n)]$. As in the ambient-pressure case, the self-energy exhibits its largest magnitude at the lowest Matsubara frequencies and gradually decreases toward zero with increasing frequency. This trend reflects the typical behavior of correlated metallic systems within DMFT: strong dynamical renormalization governs the low-energy quasiparticle regime, whereas high-frequency excitations progressively recover a more weakly interacting character. Importantly, the overall structure of the curve remains smooth and continuous, indicating that hydrostatic compression does not disrupt the coherent metallic state but instead modifies the strength of the dynamical correlations.

A comparison with the ambient-pressure result reveals that the magnitude of $\Im[\Sigma_{5/2}(i\omega_n)]$ at low frequencies becomes slightly less negative under compression. Physically, this change signals a modest reduction of the effective many-body scattering rate experienced by the $j = 5/2$ quasiparticles. Such behavior is consistent with the pressure-induced enhancement of orbital overlap and hybridization between uranium $5f$ states and surrounding ligand orbitals. As compression reduces the interatomic distances, the hybridization strength increases, which promotes more efficient dynamical screening of the local Coulomb interaction and consequently weakens the effective correlation strength acting on the low-energy quasiparticles.

The inset of Fig. SM15 magnifies the low-frequency region near $\omega_n \to 0$. In this regime the self-energy exhibits a clear linear dependence on Matsubara frequency, which is the defining signature of a Fermi-liquid state. The preservation of this linear behavior under compression indicates that the fundamental quasiparticle picture remains valid at $P = 4.427$ GPa. The red circles mark the lowest Matsubara frequencies used to perform the linear fit within the Fermi-liquid regime. Applying the standard expansion of the self-energy around zero frequency yields

$$\Im[\Sigma_{5/2}(i\omega_n)] = -0.122 - 0.841\,\omega_n, \tag{SM20}$$

from which the quasiparticle renormalization factor is obtained as $Z \approx 0.543$. The corresponding effective mass enhancement is therefore $m^*_{5/2}/m_{5/2} = Z^{-1} \approx 1.841$.

When compared with the ambient-pressure value ($Z \approx 0.522$, $m^*/m \approx 1.917$), the present result indicates a modest increase in the quasiparticle weight accompanied by a slight reduction of the effective mass. This quantitative change confirms that hydrostatic compression weakens the degree of correlation-induced renormalization within the $j = 5/2$ manifold. In other words, the $5f$ electrons acquire a somewhat more itinerant character as pressure enhances their hybridization with the surrounding conduction states.

These findings are fully consistent with the broader electronic-structure trends identified in the density-of-states and hybridization analyses. There, pressure was shown to strengthen the $5f$–ligand coupling and broaden the conduction environment surrounding the correlated uranium orbitals. The corresponding reduction of the self-energy slope observed here represents the dynamical counterpart of this increased hybridization: stronger coupling to the itinerant bath enhances electronic screening and stabilizes more coherent quasiparticle excitations.

Overall, the Matsubara self-energy analysis demonstrates that the correlated metallic state of UP_2 remains robust under hydrostatic compression while gradually evolving toward a more coherent regime. The $j = 5/2$ quasiparticles, which dominate the low-energy electronic structure, experience a moderate reduction in correlation strength and a corresponding increase in itinerancy. This behavior establishes an important reference point for evaluating the pressure response

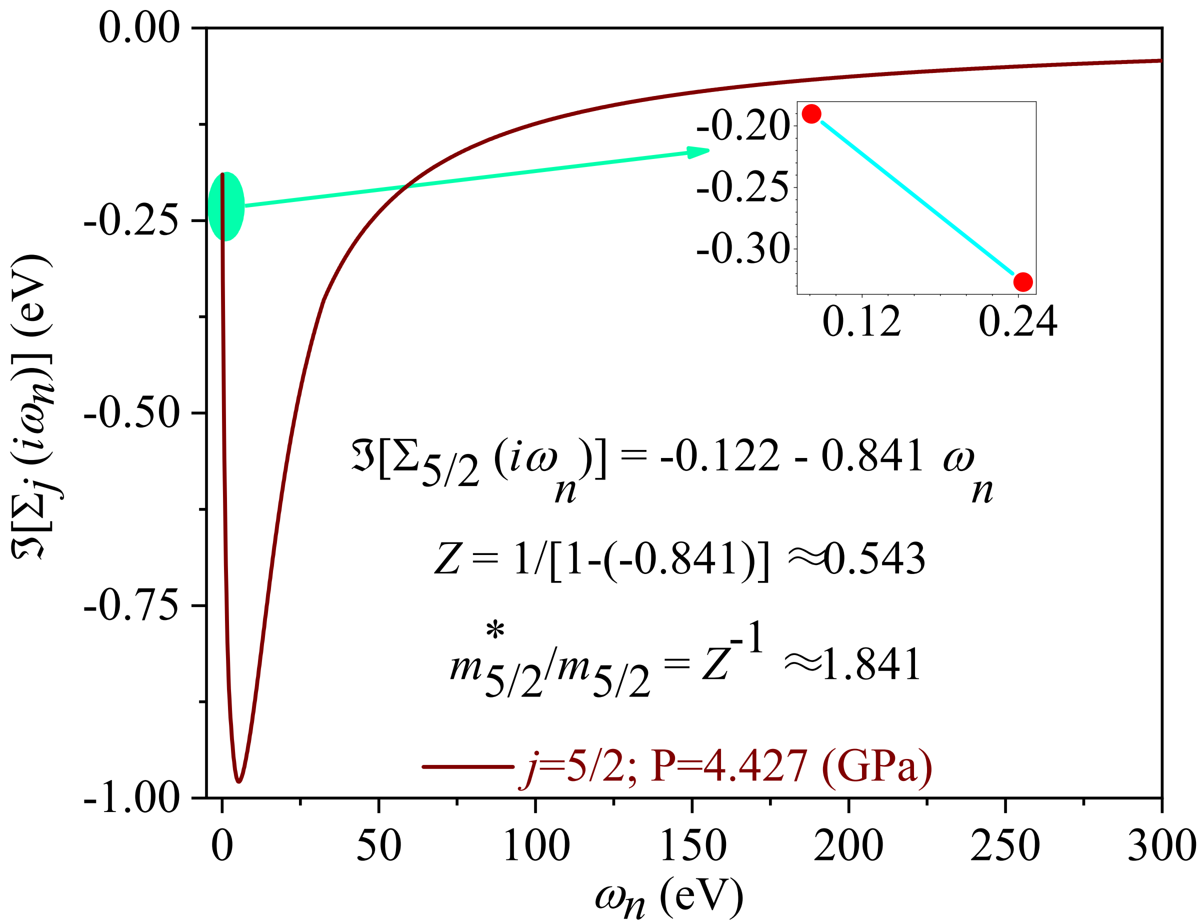

FIG. SM15. The imaginary part of the uranium $5f$ Matsubara self-energy, $\Im[\Sigma_{5/2}(i\omega_n)]$, under hydrostatic compression at $P = 4.427$ GPa. The curve is obtained from fully charge-self-consistent DFT+DMFT calculations using PBE–GGA and including SOC. The inset enlarges the low-frequency region near $\omega_n = 0$, where the self-energy displays a linear Fermi-liquid dependence. Red circles mark the Matsubara frequencies used for the linear fit, yielding $\Im[\Sigma_{5/2}(i\omega_n)] = -0.122 - 0.841\,\omega_n$. The quasiparticle weight Z is extracted according to Eq. (A3) of the main paper, consistent with the formal definition introduced in the main paper [Eq. (A2) of the main paper]. The resulting values are $Z \approx 0.543$ and $m^*_{5/2}/m_{5/2} = Z^{-1} \approx 1.841$.

of the higher-energy $j = 7/2$ manifold, whose dynamical evolution is examined in the following figure.

Figure SM16 [Fig. B1(c_4) of the main paper] completes the Matsubara self-energy analysis by presenting the pressure evolution of the uranium $5f$ $j = 7/2$ manifold at $P = 4.427$ GPa. Together with the preceding panels, this figure allows a direct comparison between the two spin–orbit–split sectors of the $5f$ shell and reveals how hydrostatic compression affects the dynamical correlation strength in the higher-energy $j = 7/2$ states. The overall Matsubara-frequency dependence of $\Im[\Sigma_{7/2}(i\omega_n)]$ remains smooth and monotonic at intermediate frequencies, while the low-frequency limit exhibits a clear linear regime characteristic of a well-defined Fermi-liquid state. This behavior indicates that even under compression the $j = 7/2$ electrons remain part of the coherent metallic state rather than forming localized excitations. The inset highlights the first Matsubara points used to determine the linear slope in the Fermi-liquid regime, from which the quasiparticle renormalization factor is extracted using Eq. (A3) of the main paper and the formal definition provided in Eq. (A2) of the main text. The linear fit yields

$$\Im[\Sigma_{7/2}(i\omega_n)] = -0.194 - 0.204\,\omega_n, \tag{SM21}$$

corresponding to a quasiparticle weight $Z \approx 0.831$ and a mass enhancement $m^*_{7/2}/m_{7/2} \approx 1.204$. These values confirm that the $j = 7/2$ sector experiences significantly weaker dynamical renormalization than the $j = 5/2$ manifold discussed in the previous panels, consistent with the fact that the $j = 7/2$ states lie predominantly away from the Fermi level and therefore couple less strongly to the low-energy quasiparticle resonance. Comparing the compressed and ambient-pressure cases reveals that the $j = 7/2$ renormalization is only modestly affected by pressure, reflecting the more itinerant character of these states and their reduced sensitivity to the hybridization-driven coherence effects that primarily control the $j = 5/2$ channel. When viewed together

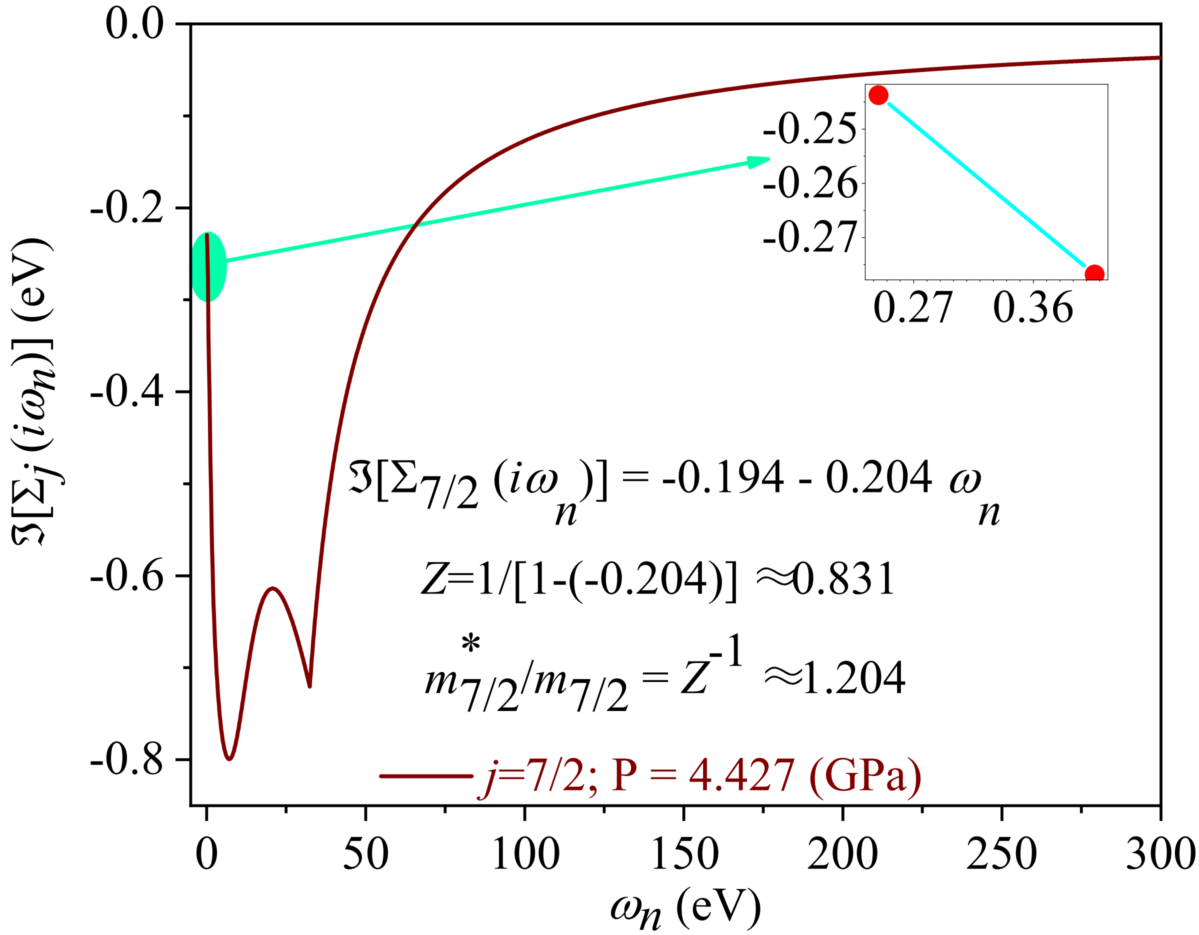

FIG. SM16. The imaginary part of the uranium $5f$ Matsubara self-energy, $\Im[\Sigma_{7/2}(i\omega_n)]$, under hydrostatic compression at $P = 4.427$ GPa obtained from fully charge-self-consistent DFT+DMFT calculations using PBE–GGA and including spin–orbit coupling. The inset enlarges the low-frequency region near $\omega_n \to 0$ where the self-energy exhibits a linear Fermi-liquid dependence. The red circles denote the Matsubara points used for the linear fit, yielding $\Im[\Sigma_{7/2}(i\omega_n)] = -0.194 - 0.204\,\omega_n$. The quasiparticle renormalization factor is extracted using Eq. (A3) of the main paper, consistent with the formal definition given in Eq. (A2) of the main text. The resulting quasiparticle parameters are $Z \approx 0.831$ and $m^*_{7/2}/m_{7/2} = Z^{-1} \approx 1.204$.

with the pressure evolution of the hybridization functions and the density of states, the Matsubara analysis establishes a coherent physical picture in which hydrostatic compression mainly strengthens quasiparticle coherence in the $j = 5/2$ sector while leaving the already weakly correlated $j = 7/2$ manifold comparatively unchanged. The hierarchy of quasiparticle renormalization therefore persists across pressure, confirming that the low-energy electronic structure of UP_2 is governed by a spin–orbit–selective correlation mechanism in which the $j = 5/2$ states dominate the correlated quasiparticle dynamics.

Building on the pressure evolution of the local dynamical correlations through the Matsubara self-energy and the corresponding quasiparticle renormalization factors, we now turn to the momentum-resolved electronic structure of UP_2. While the self-energy analysis provides a direct measure of the strength of electronic correlations in each spin–orbit channel, the momentum-resolved spectral function $A(\mathbf{k},\omega)$ reveals how these local many-body effects reshape the dispersive quasiparticle bands throughout the Brillouin zone. In particular, the spectral function allows us to visualize the formation of coherent quasiparticle states near the Fermi level, the redistribution of spectral weight between the $j = \frac{5}{2}$ and $j = \frac{7}{2}$ manifolds, and the evolution of band dispersions under hydrostatic compression. The following subsection therefore examines the pressure dependence of $A(\mathbf{k},\omega)$ in the tetragonal $I4/mmm$ phase in order to directly connect the previously extracted quasiparticle renormalization factors with the emergence of pressure-enhanced quasiparticle coherence in the interacting band structure.

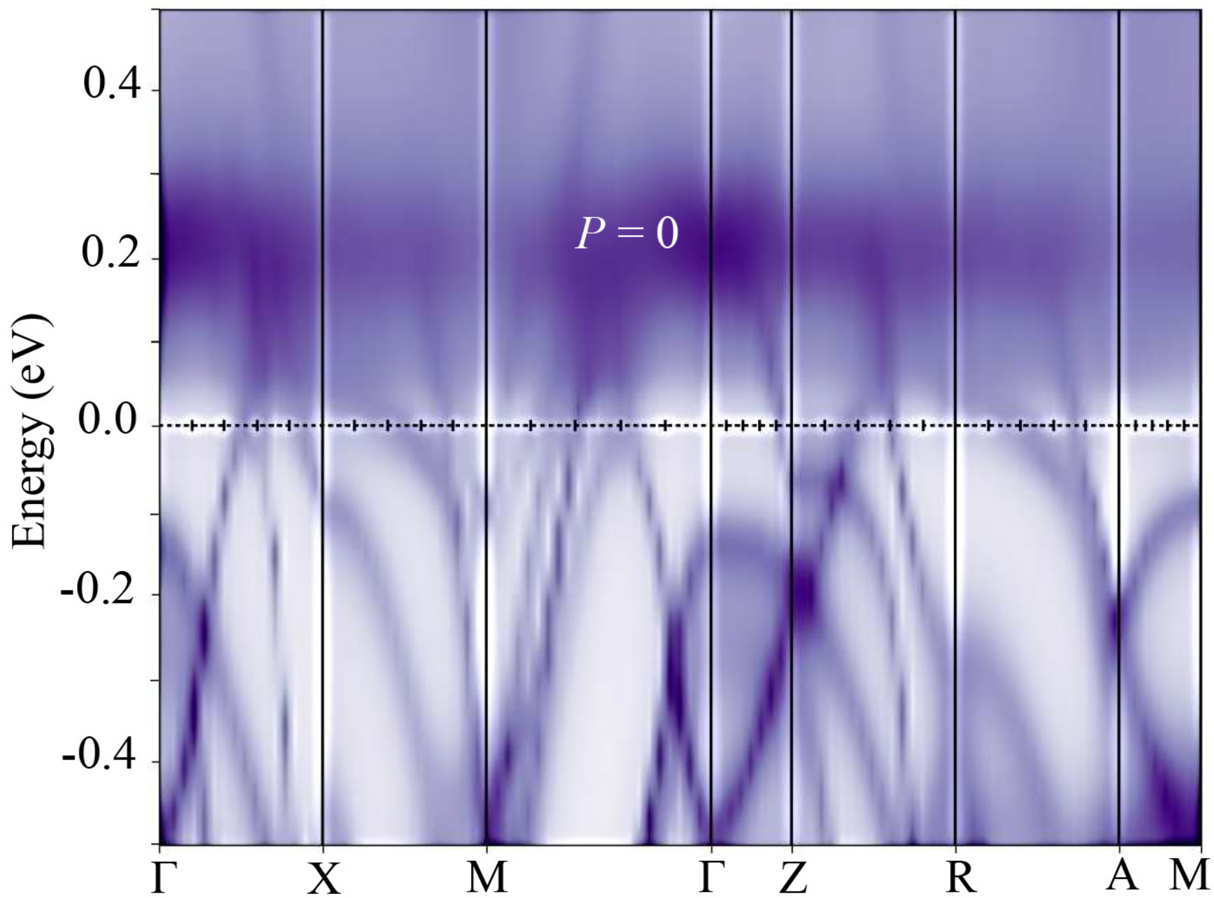

FIG. SM17. Momentum-resolved spectral function $A(\mathbf{k},\omega)$ for UP_2 in the tetragonal $I4/mmm$ phase at ambient pressure ($P=0$). The spectral intensity is computed from the interacting lattice Green's function [Eq. (5) of the main paper] through the spectral representation [Eq. (7) of the main paper], incorporating the full dynamical self-energy from the charge–self–consistent DFT+DMFT framework. The color map illustrates the quasiparticle spectral weight along the high-symmetry path Γ–X–M–Γ–Z–R–A–M–Γ. The horizontal dashed line denotes the Fermi level ($E_F=0$). Spin–orbit coupling (SOC) splits the uranium $5f$ manifold into $j=5/2$ and $j=7/2$ submanifolds; the $j=5/2$ states contribute the sharp, dispersive bands crossing the Fermi level, while the $j=7/2$ states are shifted to higher energies (visible as the diffuse weight around 0.2–0.4 eV). All calculations were performed using charge–self–consistent DFT+DMFT using PBE–GGA and including SOC.

SM I. Momentum-Resolved Spectral Function and Pressure-Enhanced Quasiparticle Coherence

Figure SM17[Fig. B2(a) of the main paper] displays the momentum-resolved spectral function $A(\mathbf{k},\omega)$ of UP_2 in the tetragonal $I4/mmm$ phase at ambient pressure ($P=0$). Because the spectral intensity is obtained from the interacting lattice Green's function [Eq. (5) of the main paper] through the spectral representation [Eq. (7) of the main paper], the resulting spectrum incorporates the full dynamical self-energy generated within the charge–self–consistent DFT+DMFT framework. Consequently, the figure directly visualizes how electronic correlations reshape the quasiparticle band structure across the Brillouin zone along the high-symmetry path Γ–X–M–Γ–Z–R–A–M–Γ.

A prominent feature of the spectrum is the presence of several dispersive bands crossing the Fermi level (horizontal dashed line), demonstrating that the $I4/mmm$ phase of UP_2 is metallic. The quasiparticle bands remain well defined across the Brillouin zone, which is consistent with the Fermi-liquid behavior inferred from the Matsubara self-energy analysis and the linear behavior of the self-energy at low frequencies as described by Eq. (A2) of the main paper. At the same time, the finite linewidths and moderate narrowing of the bands relative to typical DFT dispersions indicate the presence of appreciable many-body renormalization arising from the uranium $5f$ electrons. This coexistence of coherent band dispersion and correlation-induced renormalization is a hallmark of correlated itinerant f-electron systems.

The spectral weight near the Fermi level is dominated by uranium $5f$ states. When spin–orbit coupling is included, the $5f$ manifold splits into the $j=5/2$ and $j=7/2$ submanifolds, producing a clear hierarchy in the low-energy electronic structure. The narrow quasiparticle features concentrated around E_F originate predominantly from the $j=5/2$ states, which form a coherent resonance extending throughout momentum space. In contrast, the $j=7/2$ states appear primarily at somewhat higher energies (above 0.2 eV) and contribute less spectral intensity at the Fermi level. This orbital hierarchy mirrors the behavior observed in the orbital-resolved density of states and is consistent with the self-energy analysis, where the $j = 5/2$ channel exhibits stronger correlation effects and larger quasiparticle mass enhancement.

The dispersive character of the bands below the Fermi level further indicates substantial hybridization between the uranium $5f$ orbitals and surrounding conduction states. This hybridization produces itinerant quasiparticle bands rather than localized atomic-like excitations and leads to the formation of a coherent low-energy electronic structure. The narrow spectral ridge centered near E_F can therefore be interpreted as the momentum-resolved manifestation of the many-body quasiparticle peak that appears in the local density of states, reflecting the emergence of correlated heavy quasiparticles within the DMFT description.

Overall, the spectral function at ambient pressure reveals that UP_2 in the $I4/mmm$ structure resides in a correlated metallic regime characterized by coherent quasiparticles derived primarily from the spin–orbit–split uranium $5f$ manifold. The dominance of the $j = 5/2$ states at low energy establishes the microscopic origin of the metallic Fermi surface, while the finite linewidths and moderate renormalization encode the influence of electronic correlations. This ambient-pressure spectrum therefore provides the reference electronic structure against which the pressure-induced modifications of quasiparticle coherence and band dispersion, examined in the following panel, can be directly compared.

Figure SM18 [Fig. B2(b) of the main paper] presents the momentum-resolved spectral function $A(\mathbf{k}, \omega)$ of UP_2 at $P = 4.427$ GPa, corresponding to the same $I4/mmm$ structure as in Fig. SM17 but under finite hydrostatic compression. The band dispersions now reveal several qualitative and quantitative departures from the ambient-pressure case that directly trace the pressure evolution of the correlated uranium $5f$ electrons.

Compared with the $P = 0$ spectrum, the quasiparticle bands near the Fermi level have become noticeably narrower and more dispersive at the same time, leading to higher curvature and finer definition of the low-energy features across the Γ–M and Z–R segments. This change reflects the dual effect of pressure: (i) an increase in the effective hybridization between uranium $5f$ and ligand states, and (ii) a reduction of the quasiparticle scattering rate, manifested by the smaller imaginary component of the self-energy. These combined effects transform the electronic structure from a moderately renormalized itinerant metal into a distinctly more coherent Fermi liquid.

A second major modification is the redistribution of spectral weight between the spin-orbit components. The $j = 5/2$ manifold, which dominates the low-energy electronic structure, displays enhanced intensity directly at the Fermi level and a visibly extended momentum spread of its quasiparticle ridge. This indicates that a larger portion of the f spectral weight participates in coherent hybridization with conduction bands upon compression. The associated increase in low-energy f spectral density is consistent with the rise in the quasiparticle residue Z extracted from the self-energy analysis. By contrast, the spectral weight associated with the $j = 7/2$ manifold, centered around 0.2–0.3 eV, shifts slightly downward in energy and becomes more sharply defined, showing that pressure weakens the effective spin-orbit-induced energy separation between the two manifolds. This slight narrowing of the $j = 7/2$–$j = 5/2$ gap implies that compression enhances inter-manifold hybridization, leading to partial mixing of their spectral characters in regions near the top of the valence band.

Furthermore, the quasiparticle dispersions below E_F (seen most clearly along Γ–X–M–Γ) gain additional curvature under pressure, particularly in the strongly hybridized segments where the $5f$ states intersect the ligand-derived bands. This increased curvature implies a reduction in the effective mass of the low-energy carriers, in excellent agreement with the moderate decrease of m^*/m obtained from the Matsubara fits. The reduction of the effective mass also contributes to the enhanced spectral sharpness around E_F, strengthening the interpretation of pressure as a tuning parameter that promotes itinerant 5f behavior.

Importantly, the pressure-induced evolution is not purely uniform across momentum space. The enhancement of coherence is most pronounced along paths that involve substantial f–ligand overlap (e.g., along Γ–M and Z–R), while at high-symmetry points with limited hybridization, such as near X and A, the spectral width remains relatively unchanged. This momentum selectivity highlights the anisotropic nature of the hybridization processes that drive coherence in tetragonal UP_2 under compression. Such selective enhancement provides a microscopic explanation for the persistence of correlation-induced spectral broadening in some momentum sectors even when overall itinerancy increases.

Together, these pressure-driven changes reveal a continuous evolution rather than an abrupt transition. The compressed phase retains the spin–orbit-split $5f$ character of the ambient system but exhibits substantially stronger hybridization-driven coherence. The $j = \frac{5}{2}$ manifold gains greater spectral dominance near E_F, while the $j = \frac{7}{2}$ sector becomes slightly more itinerant due to hybridization-mediated energy shifts. Thus, hydrostatic pressure in UP_2 primarily enhances bandwidth and coherence, modestly renormalizes the SOC splitting, and redistributes spectral intensity toward low energies, all of which collectively signify a pressure-induced suppression of electronic localization.

Beyond mapping the quasiparticle dispersions, the momentum-resolved spectrum also encapsulates the underlying evolution of local many-body interactions within the uranium $5f$ shell. In particular, the coherency gain observed in Fig. SM18 originates from changes in the statistical weighting of atomic configurations within the DMFT impurity problem. The following section therefore complements the spectral analysis by examining these configuration probabilities from the CT–QMC solver, linking them quantitatively to the pressure evolution of charge fluctuations and hybridization strength that stabilize the correlated metallic state of UP_2.

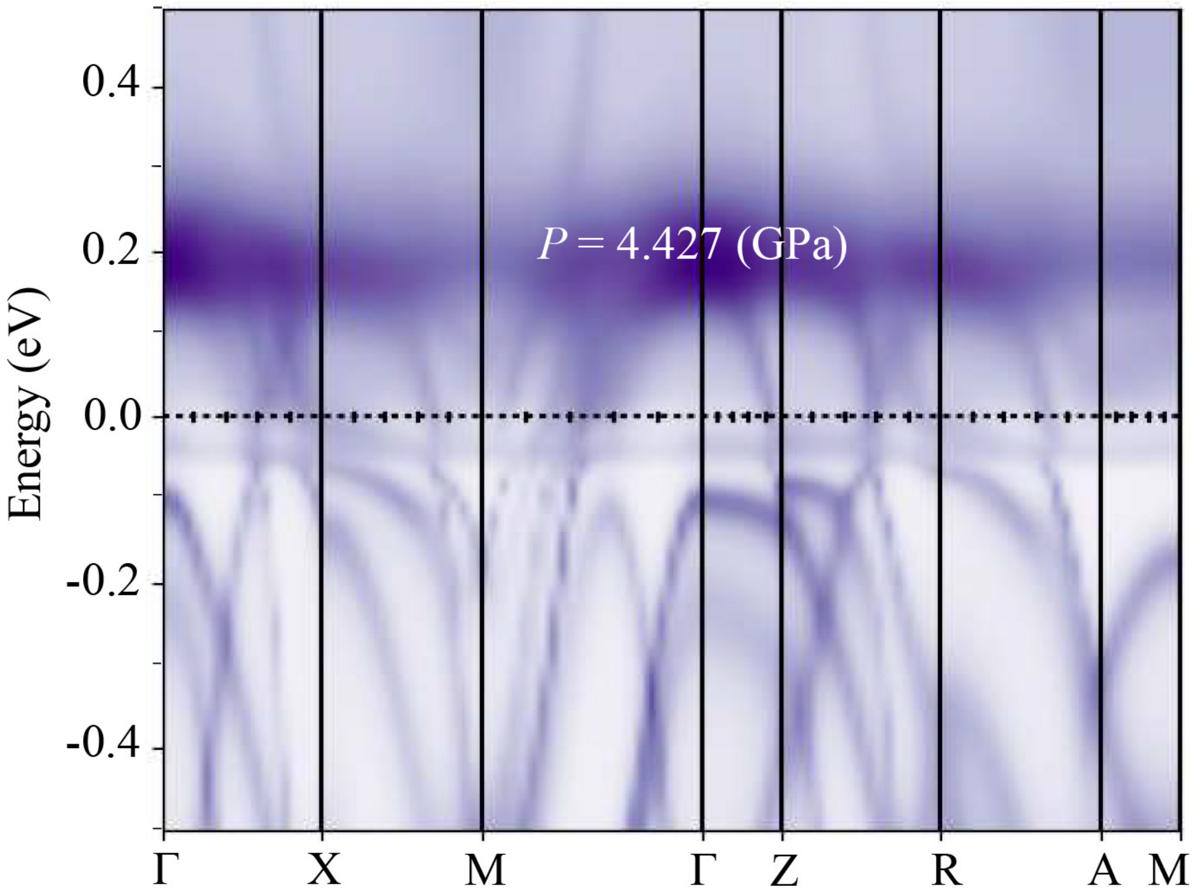

FIG. SM18. Momentum-resolved spectral function $A(\mathbf{k},\omega)$ of UP_2 in the tetragonal $I4/mmm$ phase under hydrostatic compression at $P = 4.427$ GPa. The spectral intensity is computed from the interacting lattice Green's function [Eq. (5) of the main paper] using the spectral representation [Eq. (7) of the main paper], fully incorporating the dynamical self-energy obtained within the charge–self–consistent DFT+DMFT framework using PBE–GGA and including SOC. The color map shows the evolution of the quasiparticle spectral weight along the high-symmetry path Γ–X–M–Γ–Z–R–A–M–Γ. The horizontal dashed line marks the Fermi level. Under pressure, the uranium $5f$ manifold remains split into the $j = \frac{5}{2}$ and $j = \frac{7}{2}$ submanifolds; however, the $j = \frac{5}{2}$-derived states become markedly more coherent and extended in momentum space, signaling enhanced itinerancy induced by compression.

SM II. Valence-State Statistics and Hybridization-Driven Charge Fluctuations

Figure SM19 [Fig. B2(c) of the main paper] provides a microscopic view of the uranium $5f$ configuration space in the tetragonal $I4/mmm$ phase of UP_2 at ambient pressure. Within DMFT, the CT–QMC impurity solver samples the entire manifold of atomic many-body states, and the resulting distribution of probabilities p_Γ encodes the strength of charge fluctuations, hybridization, and the degree of mixed valence. This figure therefore constitutes the statistical foundation underlying the single-particle spectra, quasiparticle masses, and hybridization effects discussed in the main text.

The probability histogram reveals that the uranium ion in UP_2 does not reside in a narrowly defined atomic configuration but instead fluctuates broadly among several $5f^N$ sectors. The dominant contributions arise from the $5f^2$ and $5f^3$ configurations, which together account for more than 85% of the total weight, as summarized in the inset pie chart. This bimodal distribution indicates a clear intermediate-valence regime: the uranium $5f$ shell is neither strictly localized (as in a purely $5f^2$ configuration) nor fully itinerant (as would be reflected in a sharply peaked $5f^3$ distribution). Instead, the DMFT solution identifies a dynamic admixture of these charge sectors, consistent with substantial $5f$–ligand hybridization and the presence of a coherent quasiparticle resonance at the Fermi level.

In addition to the dominant $5f^2$ and $5f^3$ sectors, the figure shows finite occupation of the $5f^1$ and $5f^4$ configurations. Although these contributions are smaller in magnitude, their existence is significant: they represent residual charge-transfer fluctuations, reflecting the continuous exchange of electrons between the $5f$ shell and the surrounding conduction states. Such higher- and lower-valence excursions contribute appreciably to the variance of the $5f$ occupancy, δn_f^2, and therefore to the renormalized low-energy physics. The near absence of $5f^0$ and $5f^5$ components (omitted from the histogram for clarity) confirms that these fluctu-

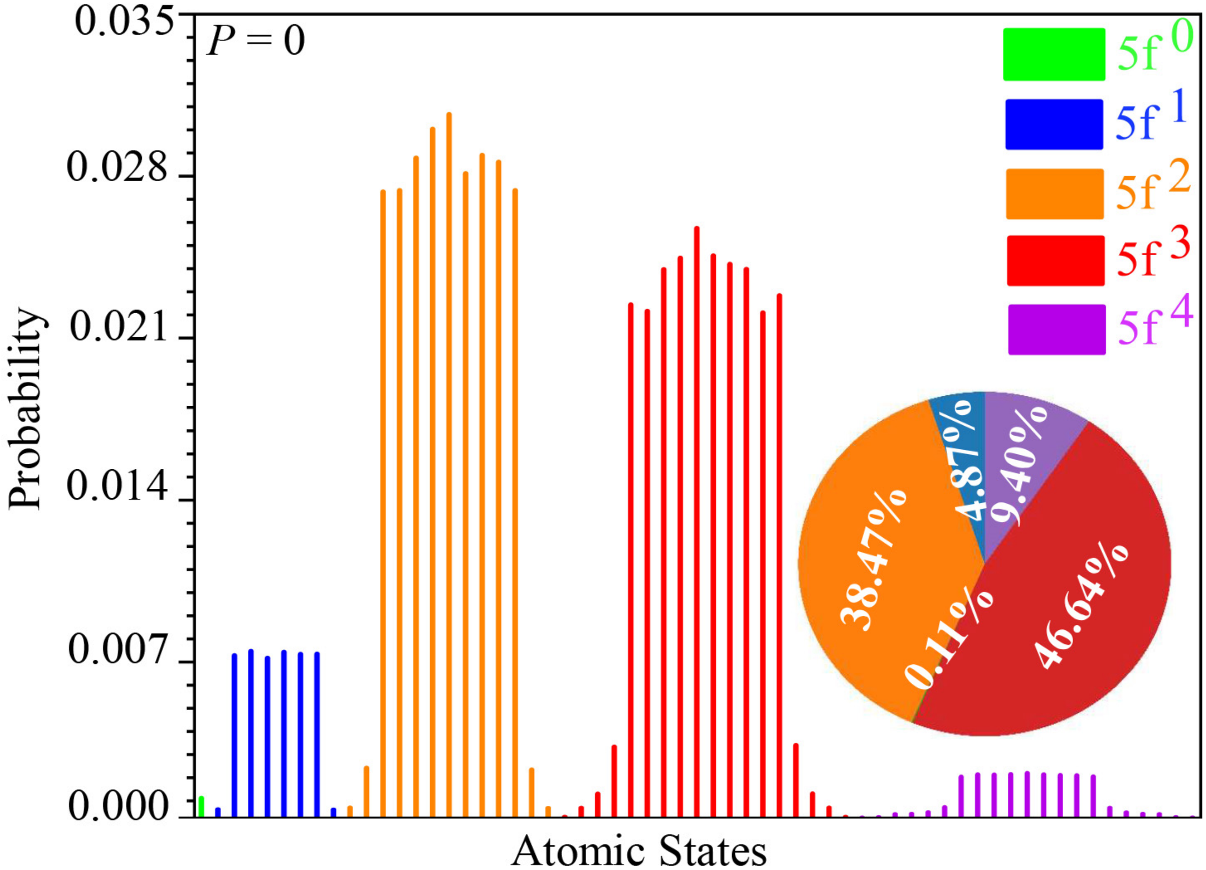

FIG. SM19. Valence-state histogram of the uranium $5f$ shell in UP_2 ($I4/mmm$) at ambient pressure ($P = 0$), obtained from the CT–QMC impurity solver within the fully charge–self–consistent DFT+DMFT framework including spin–orbit coupling (SOC). The bar plots show the statistical probabilities p_Γ of the atomic $5f^N$ configurations ($N = 0$–4), which determine the average $5f$ occupancy and the charge-fluctuation amplitude according to Eq. (9) of the main paper. The inset pie chart displays the integrated probability weight of each $5f^N$ sector. The dominant $5f^2$ and $5f^3$ contributions (38.47% and 46.64%, respectively) reveal the mixed-valence character of uranium in this phase, while the finite $5f^1$ (4.87%) and $5f^4$ (9.40%) components reflect residual charge-transfer fluctuations. The $5f^0$ contribution is negligible (0.11%) and the $5f^5$ sector is omitted due to vanishing weight. Bars are color-coded according to the total-angular-momentum j character of the associated many-body states, highlighting the SOC-resolved multiplet structure of the correlated $5f$ manifold.

ations remain within a physically meaningful and chemically realistic valence window.

Another important feature of Fig. SM19 is the color-coded internal structure within each $5f^N$ sector, which distinguishes the contributions of individual many-body states grouped by their total angular momentum j. This SOC-resolved multiplet decomposition highlights the central role of spin–orbit coupling in shaping the correlated $5f$ manifold. Rather than collapsing onto a single dominant multiplet, the probability weight is distributed among several j-resolved states, underscoring the multiorbital, strongly entangled nature of the uranium impurity problem. The system samples a wide manifold of SOC-entangled multiplets, reflecting the fact that the uranium ion in UP_2 behaves as an open quantum subsystem that dynamically explores a high-dimensional correlated state space.

Altogether, the valence statistics at $P = 0$ paint a consistent microscopic picture of UP_2 as a mixed-valent $5f$ system with substantial dynamical charge fluctuations and strong SOC-driven multiplet entanglement. These fluctuations enhance hybridization, stabilize the coherent metallic state, and set the stage for the pressure evolution analyzed in Fig. SM20. The ambient-pressure configuration histogram thus provides a crucial baseline for understanding how compression modifies the charge dynamics and reshapes the $5f$ manifold of UP_2.

Figure SM20 [Fig. B2(d) of the main paper] illustrates how hydrostatic compression modifies the many-body configuration landscape of the uranium $5f$ shell. Compared with the ambient-pressure distribution shown in Fig. SM19, the probability histogram reveals a systematic redistribution of statistical weight among the $5f^N$ sectors, reflecting the pressure-enhanced hybridization between uranium $5f$ states and the surrounding conduction bands.

The most prominent change is the reduction of the $5f^2$ contribution from about 38.5% at ambient pressure to 34.1% at $P = 4.427$ GPa, accompanied by a simultaneous increase of the $5f^4$ sector from roughly 9.4% to 12.8%. In contrast,

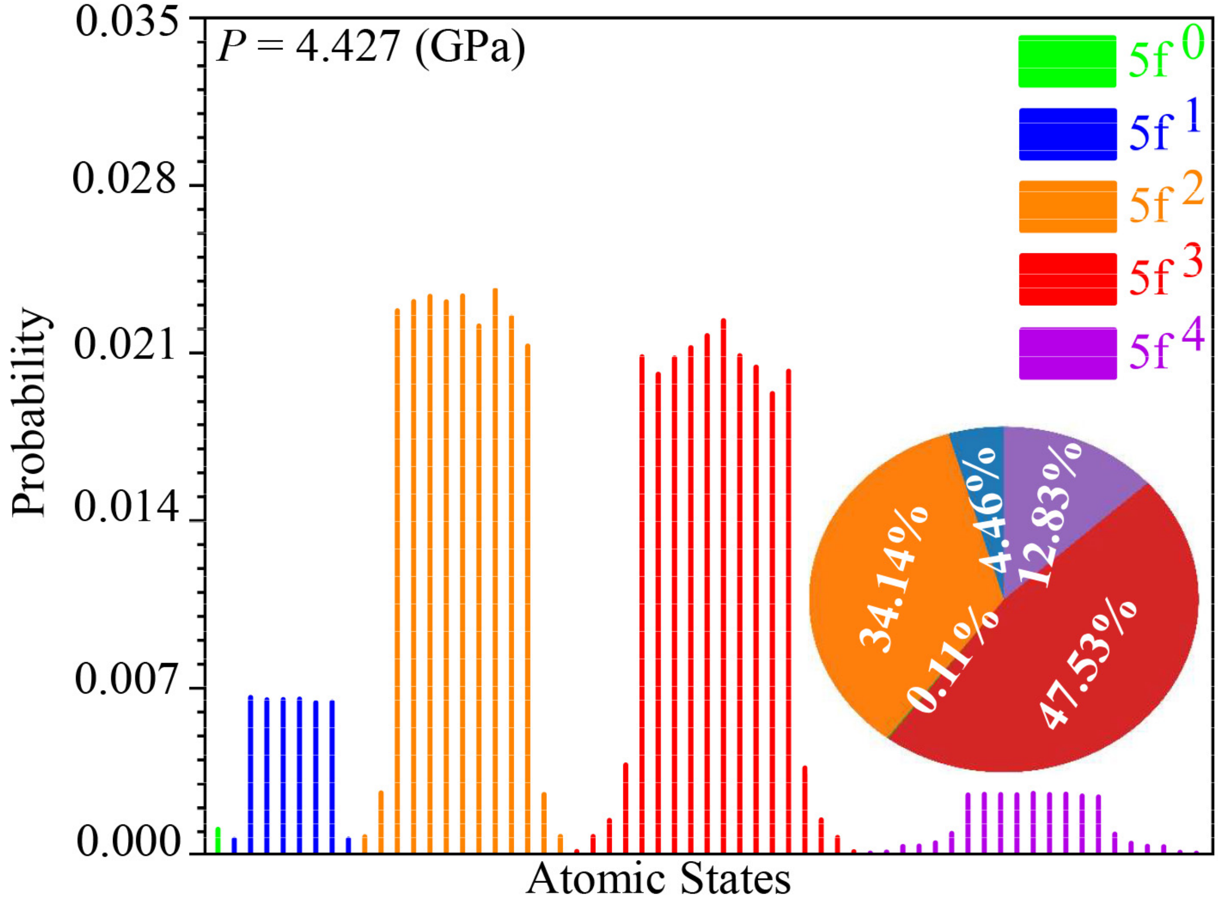

FIG. SM20. Valence-state histogram of the uranium $5f$ shell in UP_2 ($I4/mmm$) under hydrostatic compression at $P = 4.427$ GPa, obtained from the CT–QMC impurity solver within the fully charge–self–consistent DFT+DMFT framework including spin–orbit coupling (SOC). The bar plots show the statistical probabilities p_Γ of atomic $5f^N$ configurations ($N = 0$–4), which determine the average $5f$ occupancy and the amplitude of charge fluctuations according to Eq. (9) of the main paper. The inset pie chart summarizes the integrated probability weight of each $5f^N$ sector. The $5f^3$ configuration remains dominant (47.53%), while the $5f^2$ contribution decreases to 34.14%. Finite $5f^1$ (4.40%) and enhanced $5f^4$ (12.83%) weights indicate strengthened charge-transfer fluctuations under compression, whereas the $5f^0$ contribution is negligible (0.11%) and the $5f^5$ sector is omitted due to vanishing probability. Bars are color-coded according to the total angular-momentum j character of the many-body states, highlighting the SOC-resolved multiplet structure of the correlated $5f$ shell.

the $5f^3$ configuration remains the dominant component and even slightly increases its statistical weight, reaching approximately 47.5%. The persistence of a strong $5f^3$ component confirms that the uranium ion continues to fluctuate primarily between the $5f^2$ and $5f^3$ charge sectors. However, the enhanced population of the higher-valence $5f^4$ configuration clearly signals an increased tendency toward electron delocalization under compression.

This redistribution of configuration weights is a direct manifestation of pressure-driven hybridization effects. As the lattice contracts, the overlap between uranium $5f$ orbitals and ligand p states increases, strengthening the hybridization function that enters the DMFT impurity problem. The enhanced hybridization promotes dynamical charge exchange between the correlated $5f$ shell and the itinerant electronic bath, thereby expanding the range of accessible charge configurations. The increase of the $5f^4$ probability provides a clear statistical signature of this process, indicating that the correlated shell explores higher electron-count sectors more frequently as the hybridization strength grows.

The persistence of finite $5f^1$ weight, together with the increased $5f^4$ probability, implies that the distribution of configurations becomes slightly broader in configuration space under compression. This broadening reflects stronger charge fluctuations and is consistent with the pressure evolution of the average $5f$ occupancy and its variance discussed in the main text. Importantly, the $5f^0$ component remains negligible and the $5f^5$ sector continues to carry essentially zero probability, confirming that the valence fluctuations remain confined to a physically reasonable window centered around the $5f^{2-3}$ manifold.

The internal color-coded structure within each $5f^N$ sector again highlights the role of spin–orbit coupling in organizing the many-body multiplet landscape. Even under compression, the probability weight is distributed among several SOC-resolved multiplets rather than collapsing onto a single atomic state. This behavior emphasizes that the uranium ion remains a strongly correlated multiorbital impurity whose low-energy physics arises from the collective contribution of many SOC-entangled configurations.

Taken together, Fig. SM20 demonstrates that hydrostatic compression does not eliminate the mixed-valence character of UP_2, but instead slightly shifts the balance of charge configurations toward higher electron counts while preserving the dominant $5f^2$–$5f^3$ fluctuation channel. This pressure-induced redistribution of configuration weights provides a microscopic explanation for the enhanced itinerancy and strengthened quasiparticle coherence observed in the spectral and hybridization functions discussed earlier. The valence histogram therefore establishes a direct link between structural compression and the evolution of electronic correlations in UP_2.

While the valence histograms in Figs. SM19 and SM20 provide a statistical view of the configuration space explored by the uranium $5f$ shell, complementary information about the correlated state can be obtained from thermodynamic observables extracted from the DMFT impurity problem. In particular, the average $5f$ occupancy $\langle n_{5f} \rangle$ characterizes the effective valence of the uranium ion, whereas the local magnetic susceptibility χ_{loc} probes the persistence of dynamical local-moment fluctuations through the imaginary-time spin–spin correlation function. Together, these quantities provide a compact diagnostic of how mixed valence, charge fluctuations, and magnetic screening evolve under pressure. The corresponding DFT+DMFT results for paramagnetic UP_2 in the tetragonal $I4/mmm$ structure are summarized in Table SM1.

SM III. Thermodynamic Diagnostics of Pressure-Driven Hybridization and Dynamical $5f$ Fluctuations in UP_2

The thermodynamic observables summarized in Table SM1 provide an additional microscopic diagnostic of the correlated $5f$ electronic state in UP_2 within its experimentally established tetragonal $I4/mmm$ structure. Within the DFT+DMFT framework, these quantities offer complementary information about the charge and spin dynamics of the correlated uranium shell. The average $5f$ occupancy $\langle n_{5f} \rangle$ characterizes the effective valence state of uranium and quantifies charge fluctuations between different atomic configurations, while the local magnetic susceptibility χ_{loc} measures the strength and temporal persistence of dynamical spin fluctuations encoded in the imaginary-time spin–spin correlation function (Eq. (20) of the main text). Together, these quantities provide a thermodynamic probe of the balance between electronic correlations and hybridization that governs the intermediate-valence behavior of the uranium $5f$ subsystem.

At ambient pressure ($P = 0$ GPa), the $I4/mmm$ calculations yield $\langle n_{5f} \rangle = 2.62$ and $\chi_{\mathrm{loc}} = 65.19$. These values closely resemble those obtained for UP_2 within the $P4/nmm$ structural framework discussed in the main text ($\langle n_{5f} \rangle = 2.67$ and $\chi_{\mathrm{loc}} = 61.88$; see Table II). The differences between the two structural descriptions are therefore small: the change in occupancy amounts to only $\Delta n_{5f} = 2.67 - 2.62 = 0.05$, corresponding to a relative variation of less than 2%, while the local susceptibility differs by approximately 5%. Such small variations demonstrate that the correlated electronic state of UP_2 is largely insensitive to the subtle crystallographic differences between the two tetragonal structures. In both cases the uranium $5f$ shell resides in the same intermediate-valence regime dominated by mixed $5f^2$ and $5f^3$ configurations, consistent with the configuration histograms discussed in Sec. II C of the main text. The persistence of comparable χ_{loc} values further confirms that the characteristic dynamical moment fluctuations originate from intrinsic many-body correlations within the uranium $5f$ manifold rather than from minor structural variations.

Application of hydrostatic pressure produces systematic changes in both thermodynamic indicators. In the $I4/mmm$ structure the average $5f$ occupancy increases slightly from 2.62 to 2.71 upon compression to 4.427 GPa. The absolute increase $\Delta n_{5f} = 2.71 - 2.62 = 0.09$ corresponds to a relative change of roughly 3.4%, indicating only a modest redistribution of charge within the correlated shell. In contrast, the local magnetic susceptibility decreases substantially from $\chi_{\mathrm{loc}} = 65.19$ to 52.75, corresponding to a reduction of $\Delta\chi_{\mathrm{loc}} = 12.44$, or approximately 19%. This pronounced decrease in χ_{loc} signals a significant suppression of dynamical local-moment fluctuations under compression. A similar pressure response is obtained in the $P4/nmm$ calculations of the main text, where χ_{loc} decreases from 61.88 to 54.26 at the same pressure. The consistency of these trends across structural models confirms that the dominant effect of pressure is not a large change in valence but rather a modification of the dynamical screening of the uranium moment.

Within the DFT+DMFT formalism, this suppression of χ_{loc} can be directly attributed to the pressure-induced enhancement of $5f$–ligand hybridization. Compression reduces interatomic distances and increases orbital overlap between uranium $5f$ states and ligand p orbitals. In the DMFT impurity problem this effect appears as an increase in the hybridization function $-\mathrm{Im}\,\Delta(\omega)$ entering the impurity Dyson equation, which strengthens the dynamical coupling between the correlated $5f$ shell and the itinerant electronic bath. Enhanced hybridization promotes dynamical screening of the local moment, shortens the lifetime of spin fluctuations on the DMFT time scale, and drives the system toward a more coherent quasiparticle regime. This interpretation is consistent with the pressure-induced reduction of the imaginary part of the self-energy $\Im[\Sigma(i\omega_n)]$ and the sharpening of the low-energy $j = \frac{5}{2}$ quasiparticle features observed in the spectral functions discussed in the main text.

A complementary characterization of the fluctuating magnetism is provided by the finite-temperature dynamical local moment. For the $I4/mmm$ structure at ambient pressure we obtain $\mu_{\mathrm{U}} = 2.361\,\mu_{\mathrm{B}}$. This value agrees closely with the corresponding DFT+DMFT result obtained within the $P4/nmm$ structural framework for UP_2, $\mu_{\mathrm{U}} = 2.410\,\mu_{\mathrm{B}}$ (Table I of the main manuscript). The absolute difference, $\Delta\mu = 0.049\,\mu_{\mathrm{B}}$, corresponds to a relative variation of approximately 2.0%, in-

TABLE SM1. Average $5f$ occupancy $\langle n_{5f}\rangle$ and local magnetic susceptibility χ_{loc} for paramagnetic (PM) UP_2 in the tetragonal $I4/mmm$ structure obtained from fully charge self-consistent DFT+DMFT calculations using the PBE-GGA functional with SOC.

Compound	P (GPa)	$\langle n_{5f}\rangle$	χ_{loc}
UP_2	0	2.62	65.19
	4.427	2.71	52.75

dicating that the magnitude of the fluctuating uranium moment is only weakly sensitive to the specific tetragonal structural realization employed in the calculation. Moreover, the value obtained for $I4/mmm$–UP_2 lies within the range defined by the UX_2 series in Table I, $2.263 \le \mu_U \le 2.410\,\mu_B$.

It is important to emphasize that the PM moment obtained within DFT+DMFT represents a *dynamical* moment rather than a static ordered one. Because the DMFT impurity problem explicitly incorporates temporal spin and charge fluctuations, the corresponding angular-momentum fluctuations of the uranium $5f$ shell reflect the instantaneous amplitude of spin–orbit–entangled local moments. Consequently, the PM moment should be interpreted as a measure of fluctuating local-moment correlations above the magnetic ordering temperature rather than as a symmetry-breaking order parameter.

This distinction becomes evident when comparing the present results with the static AFM DFT moments summarized in Table I of the main text. Conventional DFT calculations yield ordered uranium moments in the range 1.27–$1.76\,\mu_B$ for UP_2, depending on the exchange–correlation functional and treatment of correlations. These smaller values arise because long-range magnetic order partially quenches the dynamical fluctuations that contribute to the instantaneous moment in the PM state. In contrast, DFT+DMFT retains these temporal fluctuations and therefore yields larger effective moments that agree closely with the experimental Curie–Weiss value $\mu_U \approx 2.50\,\mu_B$ reported for UP_2 above the ordering temperature [1].

Taken together, the thermodynamic diagnostics presented here establish a coherent microscopic picture of the correlated state in UP_2. At ambient pressure the uranium $5f$ shell forms a robust fluctuating moment of approximately $2.6\,\mu_B$ embedded within an intermediate-valence environment characterized by $\langle n_{5f}\rangle \approx 2.6$ and strong imaginary-time spin correlations. Hydrostatic compression enhances $5f$–ligand hybridization and thereby suppresses the persistence of these fluctuations, as reflected in the nearly 19% reduction of χ_{loc}. Importantly, the close quantitative agreement between the $I4/mmm$ and $P4/nmm$ calculations demonstrates that the essential dynamical properties of the uranium $5f$ shell are remarkably robust with respect to structural details. Instead, they are governed primarily by the competition between SOC-entangled atomic multiplet physics and hybridization-driven dynamical screening. Within this unified picture, ligand substitution across the UX_2 series sets the baseline localization scale by tuning the intrinsic $5f$–ligand hybridization strength, while hydrostatic pressure provides a complementary tuning parameter that enhances hybridization and drives the system toward a more coherent itinerant regime.

SMIX. APPENDIX: ATOMIC TERM SYMBOL, DEGENERACY, SPIN–ORBIT SPLITTING, AND TETRAGONAL CRYSTAL-FIELD SPLITTING OF URANIUM IN THE STRONG-SOC LIMIT

In this section we present a self-contained discussion of the term symbol, degeneracy, spin–orbit splitting, and tetragonal crystal-field splitting of uranium. Since several distinct but related descriptions are often mixed in the literature, it is important to separate them carefully. We shall distinguish three levels of description: first, the free uranium atom in the absence of both spin–orbit coupling and crystal field; second, the free uranium atom in the presence of spin–orbit coupling but still in the absence of crystal field; and third, uranium in a tetragonal crystal environment of symmetry $I4/mmm$, assuming that spin–orbit coupling is stronger than the crystal field. The last assumption means that the hierarchy of energy scales is

$$\lambda_{\mathrm{SOC}} \gg \Delta_{\mathrm{CF}}, \tag{SM22}$$

where λ_{SOC} denotes the spin–orbit coupling strength and Δ_{CF} denotes the crystal-field splitting scale. Under the condition expressed in Eq. (SM22), the physically appropriate procedure is to form the atomic spin–orbit-coupled multiplets first and then split them by the lower-symmetry crystal field.

SM I. General definition of the atomic term symbol

For an atom or ion in Russell–Saunders coupling, the spectroscopic term symbol is written as

$${}^{2S+1}L_J, \tag{SM23}$$

where S is the total spin quantum number, L is the total orbital angular momentum quantum number, and J is the total angular momentum quantum number obtained from vector coupling of $\mathbf{L}$ and $\mathbf{S}$. The spin multiplicity is therefore

$$2S+1, \tag{SM24}$$

while the orbital quantum number L is encoded spectroscopically by the letter sequence

$$S,\ P,\ D,\ F,\ G,\ H,\ I,\ K,\ L,\ \ldots \tag{SM25}$$

which corresponds to

$$L = 0,\ 1,\ 2,\ 3,\ 4,\ 5,\ 6,\ 7,\ 8,\ \ldots. \tag{SM26}$$

It is crucial to emphasize that the letter "L" appearing as a spectroscopic symbol in ${}^5L_6$ is not itself the numerical value of the orbital angular momentum; rather, according to Eq. (SM26), the spectroscopic letter L corresponds to orbital quantum number $L = 8$.

For the uranium free-atom ground term, the standard spectroscopic assignment is

$$ {}^5L_6. \tag{SM27} $$

Using Eqs. (SM23)–(SM26), one identifies

$$ 2S + 1 = 5, \qquad L = 8, \qquad J = 6, \tag{SM28} $$

and therefore

$$ S = 2. \tag{SM29} $$

The free neutral uranium atom has the spectroscopic ground term ${}^5L_6$. This free-atom term is used here only as an atomic reference for clarifying angular-momentum notation. It should not be interpreted as a fixed ionic configuration of uranium in UX_2, where the DFT+DMFT impurity solution exhibits mixed $5f^2$–$5f^3$ valence fluctuations. By contrast, in the one-electron relativistic picture relevant to DFT+DMFT, the $5f$ shell is split in the strong-SOC limit into the $j = 5/2$ and $j = 7/2$ sectors.

SM II. Free uranium atom without spin–orbit coupling and without crystal field

We begin from the idealized free atom in the simultaneous absence of spin–orbit coupling and crystal field. In this limit, the Hamiltonian is rotationally invariant in orbital space and spin space separately, so the good quantum numbers are L, S, and their projections M_L and M_S. Because there is no spin–orbit interaction, states with different J values belonging to the same LS term are not yet split. Therefore the relevant classification is simply by the LS term

$$ {}^{2S+1}L. \tag{SM30} $$

For uranium, this is the unsplit term

$$ {}^5L. \tag{SM31} $$

The degeneracy of an LS term in the absence of spin–orbit coupling is the product of the spin degeneracy and orbital degeneracy:

$$ g_{\mathrm{LS}} = (2S + 1)(2L + 1). \tag{SM32} $$

For uranium, substitution of $S = 2$ and $L = 8$ from Eqs. (SM28) and (SM29) gives

$$ g_{\mathrm{LS}} = (2 \times 2 + 1)(2 \times 8 + 1) = 5 \times 17 = 85. \tag{SM33} $$

Hence, in the free atom and in the absence of both spin–orbit coupling and crystal field, the uranium ground term ${}^5L$ is 85-fold degenerate.

This result may also be understood by counting the allowed projections explicitly. The spin projections are

$$ M_S = -S, -S + 1, \ldots, S, \tag{SM34} $$

which gives $2S + 1 = 5$ possibilities for $S = 2$, and the orbital projections are

$$ M_L = -L, -L + 1, \ldots, L, \tag{SM35} $$

which gives $2L + 1 = 17$ possibilities for $L = 8$. Since in the absence of SOC these degrees of freedom are independent, the total number of degenerate states is their product, which is precisely Eq. (SM33).

Therefore, the answer to the question "What is the term value and how many degenerate levels does uranium have in its free-atom ground state without spin–orbit coupling and without crystal field?" is:

$$ {}^5L, \qquad g = 85. \tag{SM36} $$

SM III. Free uranium atom in the presence of spin–orbit coupling but in the absence of crystal field

We now switch on the atomic spin–orbit interaction while keeping the atom in free space, so that no crystal field is present. The coupling of orbital and spin angular momenta is described by

$$ \mathbf{J} = \mathbf{L} + \mathbf{S}. \tag{SM37} $$

In quantum mechanics, Eq. (SM37) does not imply that J must equal $L + S$ only. Rather, the allowed values are

$$ J = |L - S|,\ |L - S| + 1,\ \ldots,\ L + S. \tag{SM38} $$

For uranium, using $L = 8$ and $S = 2$, one obtains

$$ J = 6, 7, 8, 9, 10. \tag{SM39} $$

Thus the unsplit LS term ${}^5L$ is resolved by spin–orbit coupling into the fine-structure multiplets

$$ {}^5L_6, \qquad {}^5L_7, \qquad {}^5L_8, \qquad {}^5L_9, \qquad {}^5L_{10}. \tag{SM40} $$

Each J multiplet in the free atom has degeneracy

$$ g_J = 2J + 1. \tag{SM41} $$

Therefore, the degeneracies of the five fine-structure multiplets in Eq. (SM40) are

$$ g_{J=6} = 13, \quad g_{J=7} = 15, \quad g_{J=8} = 17, \quad g_{J=9} = 19, \quad g_{J=10} = 21. \tag{SM42} $$

As a consistency check, the sum of these degeneracies must equal the original LS degeneracy, and indeed

$$ 13 + 15 + 17 + 19 + 21 = 85. \tag{SM43} $$

Equation (SM43) shows that spin–orbit coupling only redistributes the original 85 states among different J multiplets; it does not change the total number of states.

The conventional ground fine-structure level of the free uranium atom is

$$^{5}L_6. \tag{SM44}$$

Hence, once spin–orbit coupling is included, but still without crystal field, the free-atom ground-state degeneracy becomes

$$g_{J=6} = 2 \times 6 + 1 = 13. \tag{SM45}$$

Let us summarize the first two stages below:

$$^{5}L \xrightarrow{\text{SOC}} {}^{5}L_6 \oplus {}^{5}L_7 \oplus {}^{5}L_8 \oplus {}^{5}L_9 \oplus {}^{5}L_{10}. \tag{SM46}$$

Before SOC, the uranium free-atom ground term is 85-fold degenerate; after SOC, this degeneracy is split into five fine-structure multiplets, and the lowest among them is $^{5}L_6$ with 13-fold degeneracy.

SM IV. Important distinction between many-electron atomic terms and one-electron $5f$ spinor states

Before proceeding to the crystal case, it is essential to clarify a common source of confusion. There are two different but related descriptions of uranium $5f$ states:

First, there is the many-electron atomic-term description discussed above, in which the free atom is classified by a term symbol such as $^{5}L_6$. This is a many-body classification of the total angular momentum of the atomic ground state.

Second, there is the one-electron relativistic description of the $5f$ shell, which is the language commonly used in electronic-structure methods such as DFT, DFT+U, and DFT+DMFT. In that one-electron picture, each f electron has orbital angular momentum

$$l = 3, \tag{SM47}$$

and, including spin, the dimension of the one-electron f shell is

$$2(2l+1) = 2(7) = 14. \tag{SM48}$$

When one-electron spin–orbit coupling is included, the f shell splits into two relativistic subspaces with

$$j = l - \frac{1}{2} = \frac{5}{2}, \qquad j = l + \frac{1}{2} = \frac{7}{2}. \tag{SM49}$$

Their dimensions are

$$2j+1 = 6 \quad \text{for } j = \frac{5}{2}, \qquad 2j+1 = 8 \quad \text{for } j = \frac{7}{2}, \tag{SM50}$$

so that

$$14 = 6 + 8. \tag{SM51}$$

Equation (SM51) describes the splitting of the one-electron $5f$ shell, not the splitting of the many-electron atomic term ^{5}L. Both descriptions are useful, but they answer different physical questions. The many-electron term-symbol language is appropriate for discussing the atomic ground term and its fine structure. The one-electron $j = 5/2$ and $j = 7/2$ language is the natural basis for relativistic band-structure and DFT+DMFT calculations, including the practical interpretation of files such as case.indmfl and Trans.dat.

SM V. Uranium in a tetragonal crystal of symmetry $I4/mmm$ with strong spin–orbit coupling

We now consider uranium in a crystal with space group $I4/mmm$. The relevant point-group symmetry at a high-symmetry uranium site is tetragonal

$$D_{4h}. \tag{SM52}$$

Under the strong-SOC condition in Eq. (SM22), one should not begin from the crystal field acting on the unsplit orbital states. Instead, one first forms spin–orbit-coupled states and then lets the crystal field split them.

There are again two related viewpoints: the many-electron crystal-field splitting of the atomic $J = 6$ multiplet, and the one-electron splitting of the relativistic $5f_{5/2}$ and $5f_{7/2}$ manifolds. Since the practical computational context involves a 14-dimensional f basis, the one-electron viewpoint is particularly relevant, but for completeness we first explain the many-electron logic.

SM I. Many-electron viewpoint: splitting of the atomic $^{5}L_6$ multiplet

From the atomic point of view, the free-ion ground multiplet in the presence of SOC is $^{5}L_6$, with degeneracy

$$2J + 1 = 13. \tag{SM53}$$

In a crystal, rotational symmetry is reduced from the full rotation group to the site-symmetry group D_{4h}. Therefore the $J = 6$ multiplet is split by the tetragonal crystal field into lower-dimensional irreducible representations of the crystal symmetry group. Formally, one writes the local Hamiltonian as

$$H = H_{\text{atom}} + \lambda\, \mathbf{L} \cdot \mathbf{S} + H_{\text{CF}}, \tag{SM54}$$

where the tetragonal crystal-field Hamiltonian may be expanded in Stevens operators as

$$H_{\text{CF}} = B_2^0 O_2^0 + B_4^0 O_4^0 + B_4^4 O_4^4 + B_6^0 O_6^0 + B_6^4 O_6^4. \tag{SM55}$$

Here B_k^q are crystal-field parameters and O_k^q are Stevens operator equivalents. Diagonalization of Eq. (SM54) within the $J = 6$ manifold gives the crystal-field eigenstates and energies. Since $J = 6$ is an integer, this is not a Kramers multiplet, and symmetry does not require all levels to remain doubly degenerate. Therefore the original 13-fold degeneracy in Eq. (SM53) is lifted into a set of crystal-field singlets and, depending on the representation content, possibly non-Kramers doublets. The representation content is fixed by the site symmetry and by the value of J, whereas the crystal-field parameters determine the level energies, ordering, and the detailed composition of the eigenstates within the symmetry-allowed subspaces.

Thus, at the many-electron level, the physical picture is

$$^{5}L \xrightarrow{\text{SOC}} {}^{5}L_6 \xrightarrow{\text{CF in } D_{4h}} \text{crystal-field sublevels.} \tag{SM56}$$

SM II. One-electron viewpoint: splitting of the $5f$ shell in relativistic electronic-structure calculations

In relativistic electronic-structure approaches, one typically works instead with the one-electron $5f$ shell. In that case, Eq. (SM48) gives the 14-dimensional local space, and spin–orbit coupling first produces the two relativistic manifolds $j = 5/2$ and $j = 7/2$ in Eq. (SM49). Under the tetragonal crystal field of point group D_{4h}, these are further reduced according to the double-group irreducible representations.

Because $j = 5/2$ and $j = 7/2$ are half-integer angular momenta, time-reversal symmetry guarantees Kramers degeneracy. Therefore each resulting crystal-field level is at least twofold degenerate. The decomposition under the tetragonal double group is

$$j = \frac{5}{2} \longrightarrow \Gamma_6 \oplus \Gamma_7 \oplus \Gamma_7, \tag{SM57}$$

and

$$j = \frac{7}{2} \longrightarrow \Gamma_6 \oplus \Gamma_6 \oplus \Gamma_7 \oplus \Gamma_7. \tag{SM58}$$

Equation (SM57) means that the six states of the $j = 5/2$ manifold split into three Kramers doublets, while Eq. (SM58) means that the eight states of the $j = 7/2$ manifold split into four Kramers doublets. Consequently, the full 14-dimensional one-electron $5f$ shell becomes

$$14 \xrightarrow{\text{SOC}} 6 + 8 \xrightarrow{\text{CF in } D_{4h}} 2 + 2 + 2 + 2 + 2 + 2 + 2. \tag{SM59}$$

Thus, in the one-electron relativistic picture appropriate to DFT+DMFT, the uranium $5f$ shell in tetragonal symmetry and in the strong-SOC regime is split into seven Kramers doublets.

This is the natural interpretation of a 14-dimensional correlated subspace separated into two SOC sectors labeled $j = 5/2$ and $j = 7/2$. In practical computational files such as case.indmfl and Trans.dat, one indeed encounters this structure: the correlated shell is the f shell with $l = 3$, the spin–orbit basis separates it into $j = 5/2$ and $j = 7/2$, and the tetragonal environment further splits these subspaces without strong mixing when the hierarchy of Eq. (SM22) applies.

SM VI. Why the strong-SOC hierarchy matters

The assumption of Eq. (SM22) is not merely technical; it determines the correct order of symmetry reduction. If crystal-field splitting were stronger than spin–orbit coupling, one would first classify the orbital states under the crystal point group and only then treat SOC. But in uranium $5f$ systems the spin–orbit interaction is typically large, so the physically relevant order is

$$\begin{array}{c} \text{Atomic Shell} \\ \downarrow \text{SOC} \\ j \text{ Multiplets} \\ \downarrow \text{CF} \\ \text{Crystal-Field Sublevels} \end{array} \tag{SM60}$$

In the one-electron picture, Eq. (SM60) becomes

$$5f \xrightarrow{\text{SOC}} 5f_{5/2} \oplus 5f_{7/2} \xrightarrow{\text{CF in } D_{4h}} 7 \text{ Kramers doublets.} \tag{SM61}$$

In the many-electron atomic-term picture, the corresponding logic is

$$^5L \xrightarrow{\text{SOC}} {}^5L_6 \xrightarrow{\text{CF in } D_{4h}} \text{crystal-field sublevels.} \tag{SM62}$$

These two chains are not contradictory. They belong to two different levels of description of the same uranium physics: the first is a one-electron relativistic shell picture, and the second is a many-electron atomic-term picture.

SM VII. Summary

In short, uranium has an 85-fold degenerate LS ground term ^5L when both spin–orbit coupling and crystal field are absent. Atomic spin–orbit coupling splits this term into five fine-structure multiplets, among which the ground level is $^5L_6$ with 13-fold degeneracy. In a tetragonal crystal of symmetry $I4/mmm$, with spin–orbit coupling stronger than the crystal field, the relevant relativistic $5f$ shell first splits into the $j = 5/2$ and $j = 7/2$ sectors and is then further resolved by the tetragonal crystal field into a total of seven Kramers doublets.

CONCLUSION

In this Supplementary Material we established the numerical reliability and physical consistency of our fully charge self-consistent PBE–GGA+SOC DFT+DMFT calculations, and we validated that the main conclusions of the manuscript are robust with respect to both convergence controls and the structural refinement for UP_2. The two-level convergence analysis (outer charge-self-consistent cycle and inner impurity loop) confirms that the reported spectral, statistical, and thermodynamic observables correspond to stable paramagnetic solutions at $T = 300$ K.

Focusing on the experimentally established tetragonal $I4/mmm$ structure of UP_2, we showed that the low-energy electronic structure is dominated by a correlated U-$5f$ quasiparticle resonance with a pronounced spin–orbit hierarchy: the coherent states at E_F originate predominantly from the $j = \frac{5}{2}$ manifold, while the $j = \frac{7}{2}$ weight is largely shifted to higher energies. The corresponding valence-state statistics and thermodynamic diagnostics consistently place UP_2 in an intermediate-valence regime with mixed $5f^2$–$5f^3$ character.

Hydrostatic pressure primarily acts to enhance $5f$–ligand hybridization and quasiparticle coherence rather than to drive a valence transition. This is reflected in the weak pressure dependence of the average occupancy, $\langle n_{5f} \rangle = 2.62 \to 2.71$, contrasted by the marked reduction of the local susceptibility, $\chi_{\text{loc}} = 65.19 \to 52.75$, in Table SM1. Within DMFT, the suppression of χ_{loc} indicates enhanced dynamical screening and a shorter lifetime of local-moment fluctuations, consistent with the pressure-induced sharpening of the $j = \frac{5}{2}$ quasiparticles and the reduced scattering encoded in $\Im[\Sigma(i\omega_n)]$.

Importantly, these conclusions are quantitatively consistent across structural realizations: at ambient pressure the $I4/mmm$ values of $\langle n_{5f}\rangle$ and $\chi_{\rm loc}$ closely match those obtained in the unified $P4/nmm$ reference structure of the main text (Table II of the main paper). Likewise, the finite-temperature dynamical local moment for $I4/mmm$ UP_2, $\mu_{\rm U} = 2.361\,\mu_{\rm B}$, agrees with both the corresponding $P4/nmm$ DFT+DMFT value and the experimental Curie–Weiss moment, reinforcing the interpretation emphasized in Sec. IV A of the main paper: $\mu_{\rm U}$ and $\chi_{\rm loc}$ quantify SOC-entangled, temporally fluctuating $5f$ moments rather than static ordered moments.

We further clarified the relation between the atomic and computational descriptions of the uranium $5f$ shell by distinguishing the many-electron $^5L_6$ atomic ground term from the one-electron relativistic basis used in the DFT+DMFT implementation, where the shell is organized into $j = 5/2$ and $j = 7/2$ sectors and further split by tetragonal crystal fields in the strong-SOC regime. In addition, the complete workflow connecting the DFT+DMFT hybridization output to the CT-QMC solver input was documented explicitly, including the symmetry reduction into independent channels, the generation of `Delta.imp`, the conversion to `Delta.inp`, and the internal reconstruction of the full matrix-valued hybridization used by the impurity solver. We also presented a reproducible operator-based procedure for extracting the paramagnetic local moment from CT-QMC probability distributions, making explicit that the reported moments are dynamical impurity observables rather than isolated-atom estimates or ordered-state moments.

Overall, the dynamical moment, valence statistics, and susceptibility diagnostics form a unified physical picture. UP_2 hosts a robust, hybridization-controlled intermediate-valence $5f$ state whose low-energy properties are governed by the balance between local multiplet correlations (SOC-entangled) and hybridization-driven screening. When viewed together with the main-text UX_2 trends, these results further support a coherent materials design principle: ligand substitution primarily sets the baseline hybridization/localization scale across the series, whereas pressure provides a complementary tuning axis that enhances hybridization and suppresses the persistence of dynamical local moments within a given compound. Thus, the correlated $5f$ phenomenology identified in the $P4/nmm$ model is an intrinsic and structurally robust characteristic of UP_2, also confirmed explicitly in the experimental $I4/mmm$ phase.

[1] G. Amoretti, A. Blaise, and J. Mulak, J. Magn. Magn. Mater. **42**, 65 (1984).

[2] Z. Henkie, P. Wiśniewski, R. Fabrowski, and R. Maślanka, Solid State Commun. **79**, 1025 (1991).

[3] P. Wiśniewski, D. Aoki, N. Watanabe, R. Settai, Y. Haga, E. Yamamoto, and Y. Ōnuki, J. Phys. Soc. Jpn. **70**, 278 (2001).

[4] R. Ebrahimi-Jaberi and S. Jalali-Asadabadi, Supplementary Dataset and Computational Details Supporting the Main Article Entitled: Microscopic Mechanisms and Dual Pathways of 5f Electron Itinerancy Tuned by Ligand Chemistry and Pressure in Paramagnetic Uranium Dipnictides (2026), DFT+DMFT results in UX_2 at $T = 300$ K under ligand substitution and pressure. Includes DOS, hybridization $-\Im[\Delta(\omega)]$, spectral functions $A(\mathbf{k},\omega)$, $5f$ atomic-state probabilities, and Matsubara self-energies $\Im[\Sigma_j(i\omega_n)]$ for $j = 5/2, 7/2$. URL: https://doi.org/10.6084/m9.figshare.31967763; README: https://figshare.com/ndownloader/files/63570081.

[5] S. Tsutsui, M. Nakada, S. Nasu, Y. Haga, D. Aoki, P. Wiśniewski, and Y. Ōnuki, Phys. Rev. B **69**, 054404 (2004).

[6] E. Ghasemikhah, S. Jalali Asadabadi, I. Ahmad, and M. Yazdani-Kacoei, Rsc Adv. **5**, 37592 (2015).

[7] R. Ebrahimi-Jaberi and S. Jalali-Asadabadi, Mater. Chem. Phys. **312**, 128590 (2024).

[8] Y. Jiang, Z. Song, T. Zhu, Z. Fang, H. Weng, Z.-X. Liu, J. Yang, and C. Fang, Phys. Rev. X **14**, 031039 (2024).